Segmentation and Holocene Behavior of the Middle Strand of the North Anatolian Fault (NW Turkey)

Yacine Benjelloun, J. De sigoyer, S. Garambois, J. Carcaillet, Y. Klinger

Segmentation and Holocene Behavior of the Middle Strand of the North Anatolian Fault (NW Turkey)

Y. Benjelloun[1], J. de Sigoyer[2], S. Garambois[2], J. Carcaillet[2], and Y. Klinger[1]

[1]Université de Paris, Institut de physique du globe de Paris, CNRS, F-75005 Paris, France.

[2]Univ. Grenoble Alpes, Univ. Savoie Mont Blanc, CNRS, IRD, IFSTTAR, ISTerre, 38000 Grenoble, France.

Corresponding author: Yacine Benjelloun (benjelloun@ipgp.fr)

Key Points:

- Systematic measurements of horizontal cumulative offsets along the middle strand of the North Anatolian fault
- Statistical analysis of the dataset allows to identify the last large ruptures along the fault and the associated slip per-segment
- Comparison with independent constraints on past earthquakes leads to discuss past rupture scenarios

This article has been accepted for publication and undergone full peer review but has not been through the copyediting, typesetting, pagination and proofreading process, which may lead to differences between this version and the Version of Record. Please cite this article as doi: 10.1029/2021TC006870.

Abstract

The North Anatolian fault in the Marmara region is composed of three parallel strands all separated by ~50 km. The activity of the middle strand, which borders the southern edge of the Marmara Sea, is much debated because of its present-day very low seismicity. This contrasts with historical, archaeological and paleoseismological evidence, which suggest several destructive earthquakes have occurred during the last 2000 years. Our study aims to better constrain seismic hazard on the middle strand by exploring its Holocene paleoseismicity. For this, we mapped 148 km of the eastern part of the middle strand, using high-resolution satellite imagery. A series of landforms offset by the middle strand activity have been systematically measured to recover the past ruptures. Three Late Pleistocene-Holocene terraces have been dated with the terrestrial cosmogenic nuclide method, constraining a horizontal slip rate of $\mathbf{4.4^{+10.6}_{-2.8}}$ mm/yr. The statistical analysis of the offsets evidences several major ruptures preserved in the landscape, with coseismic lateral displacements ranging between 3 and 6.5 m. This corresponds to Mw ~7.3 earthquakes able to propagate along several fault segments. Historical seismicity and paleoseismology data suggest that the last large earthquakes along the MNAF happened in 1065 CE and between the 14th and 18th centuries CE. Since then, the MNAF may have accumulated enough stress to generate a destructive rupture.

1 Introduction

Seismic hazard in the highly inhabited areas of northwestern Turkey is mainly related to the activity of the North Anatolian fault (NAF), a ~1500-km long, dextral strike-slip structure that accommodates the relative motion between the Eurasian and Anatolian blocks (Ambraseys, 1970; Barka, 1992; Ketin, 1969; Sengör & Zabci, 2019; Sengör et al., 2005), with a total

geodetic slip estimated around 3 cm/yr (Fig. 1; McClusky et al., 2000; Meade et al., 2002). During the 20th century, the NAF ruptured almost entirely during a westward sequence of major earthquakes from Erzincan, in 1939, to Düzce and Izmit, in 1999 (Akyüz et al., 2002; Ambraseys, 2001a; Barka, 1996; Barka et al., 2002; Hubert-Ferrari et al., 2000; Stein et al., 1997). A seismic gap remains in the Sea of Marmara, in front of Istanbul, where a major earthquake is expected to occur in the next decades (Parsons et al., 2000). In addition to the main northern strand of the NAF, one should also consider the seismic hazard due to the presence of two secondary strands known as the middle and southern strands (MNAF and SNAF, Fig. 1). Although there are a large number of geodetic and geological slip rate estimates for the NNAF in the Marmara region (e.g. Dikbas et al., 2018; Ergintav et al., 2014; Grall et al., 2013; Kurt et al., 2013; Motagh et al., 2007; Reilinger et al., 2006), there are few studies for the southern strands (Zabci, 2019). These strands could together accommodate as much as 25% of the total slip of the NAF (Armijo et al., 2002; Flerit et al., 2003), with slip rates between 7 and less than 1 mm/yr on the MNAF estimated with geodetical (Ergintav et al., 2014; Özbey et al., 2021; Reilinger et al., 2006) and geological data (Gasperini et al., 2011; Özalp et al., 2013; Vardar et al., 2014). While the SNAF experienced a Mw 7.2 earthquake in 1953 (Ketin & Rösli, 1953; Kürçer et al., 2008, 2019), no major earthquake ruptured the MNAF during the instrumental period, and the seismicity of the MNAF zone during the last eight decades does not include more than a couple of earthquakes larger than Mw 5. The microseismicity recently recorded has been mostly located west of Iznik Lake and around the Gulf of Gemlik, while the other segments in the east have been characterized by much fewer events and appear quiescent compared with the neighboring NAF strands (Baris et al., 2002; Gürbüz et al., 2000; Öztürk et al., 2009; Tsukuda et al., 1988). These observations explain that the middle strand has often been overlooked in the assessment of deformation of the Marmara region (Le Pichon et al., 2014). This current quiescence contrasts

with a significant historical seismic activity documented by several chronicles mentioning the destruction of Iznik and other surrounding cities located close to the MNAF during large earthquakes occurring in the last 2000 years (Ambraseys, 2002, 2009; Ambraseys & Finkel, 1991; Ambraseys & Jackson, 1998; Guidoboni & Comastri, 2005; Fig. 2).

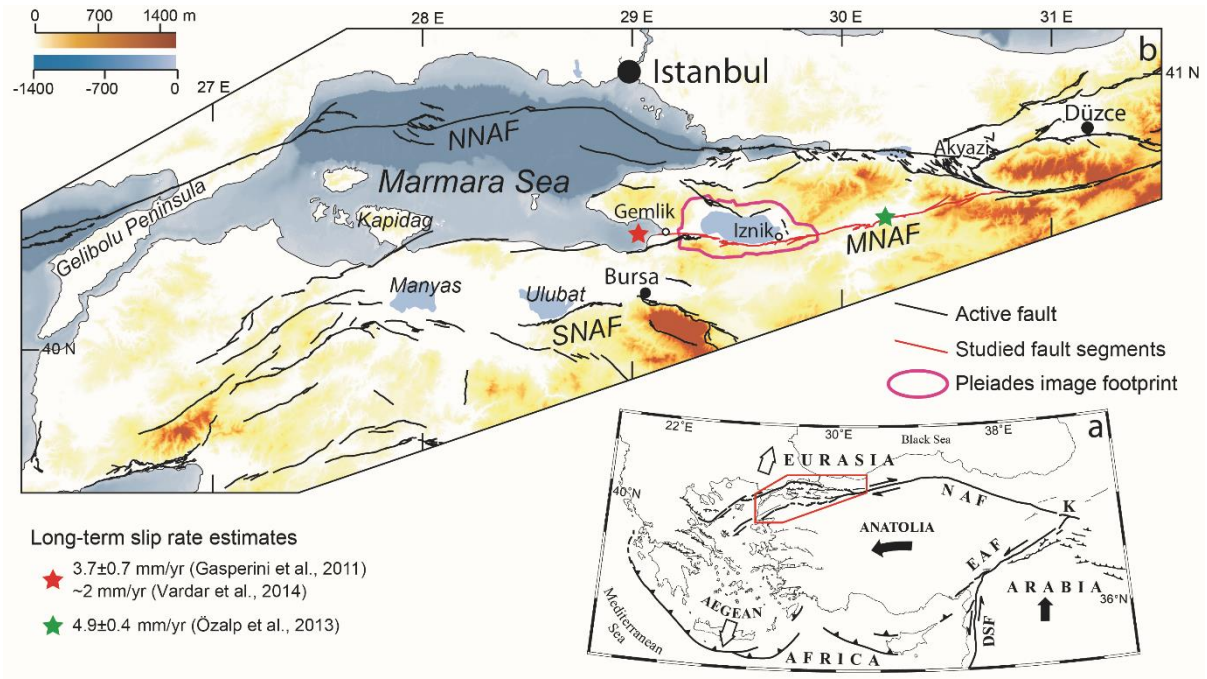

Figure 1. General tectonic context. (a) Schematic map of the main active fault zones of the Eastern Mediterranean (Armijo et al., 1999). NAF = North Anatolian fault, EAF = East Anatolian fault, DSF = Dead Sea fault. The red box surrounds the Marmara region. (b) Main active faults located within the Marmara region in black. The fault map was modified from Emre et al. (2011). NNAF, MNAF and SNAF refers to the northern, middle and southern strand of the NAF respectively. The bathymetry comes from the EMODnet Bathymetry Consortium (2018). The color stars locate fault sections where slip rates were estimated by geology or geomorphology studies (see Section 3 for details).

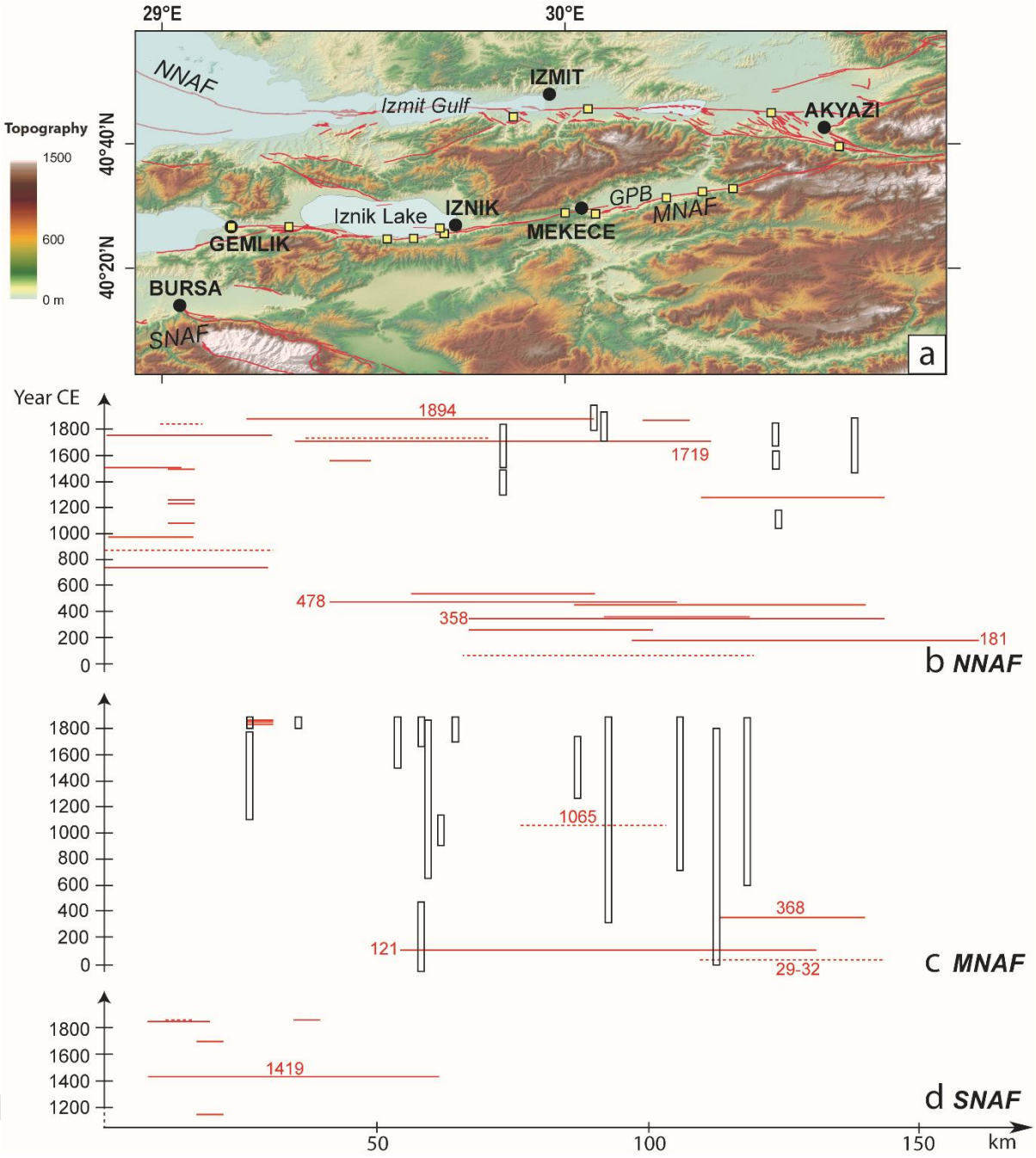

Figure 2. Historical seismicity of the eastern Marmara region before 1900 CE (Common Era). (a) Active faults and main geographic features of the Marmara region. Trench sites are located with yellow boxes. GPB=Geyve-Pamukova Basin. (b, c, d) Historical earthquakes (horizontal red lines) and seismic events documented in palaeoseismological studies (vertical boxes) along the three strands of the NAF. The horizontal lines are positioned according to the epicentral areas interpreted from the sources. These epicentral areas are determined from the

spatial distribution of the seismic intensities interpreted from historical descriptions, and their accuracy depends on the availability and quality of the written archives (Ambraseys et al., 2002). Dashed lines indicate less documented events. The length of each horizontal line corresponds to the approximate rupture length of the earthquake. To estimate this length, we rely on the magnitude estimated by historical seismology studies (see Table S1 in Supporting Information), from which a surface rupture length was derived using the relationship of Wells and Coppersmith (1984). The length of the vertical boxes corresponds to the dating of the events within 2σ uncertainty (Civico et al., 2021; Dikbas et al., 2018; Dogan, 2010; Gastineau et al., 2021; Honkura & Isikara, 1991; Ikeda, Suzuki et al., 1991; Klinger et al., 2003; Özalp et al., 2013; Rockwell et al., 2009; see Table S2 in Supporting Information for detailed data).

In the last decades, the development of high-resolution satellite imagery has made it possible to measure the deformation and characterize in great detail the geomorphology of tectonically active regions on a large scale (Elliott et al., 2016; Fu et al., 2004; Klinger et al., 2011; Ren et al., 2018). These images enable us to accurately map active faults along several tens of kilometers, to describe their segmentation and therefore provide useful information on the possible extension of a given rupture (e.g. Ansberque et al., 2016; Choi et al., 2018; Klinger et al., 2005). Such data also make it possible to document the long-term, cumulative slip distribution along the fault through inventories of offset geomorphological markers. This approach has been successfully employed since the 1960s on various faults to extract coseismic slip values from cumulative offset measurements, and to discuss the impact of segmentation in modulating the cumulative along-strike displacement (Ansberque et al., 2016; Barka, 1996; Manighetti et al., 2015, 2020; McGill and Rubin, 1999; Sieh and Jahns, 1984; Zielke et al., 2015; Kurtz et al., 2018).

In this study, we use a set of high-resolution images and topography measurements obtained

from Pleiades data to map the eastern part of the MNAF between Gemlik and Akyazi district (Fig. 2a), and to measure a series of lateral displacements recorded by geomorphological markers, mainly stream talwegs and risers. To gather additional age control on the observed cumulative deformation, we sample and date three levels of wave-cut terraces formed around Iznik Lake. This enables us to constrain a Holocene horizontal slip rate for the central section of the MNAF. A statistical analysis of the offset measurements allows us to extract coseismic displacements for several of the largest past earthquakes and to discuss the slip distribution generated along the fault during these earthquakes. Comparison of these data with the historical seismicity record and previous paleoseismological data shows that this approach is not sensitive enough to detect the smaller events (Mw 6.8-7) that are also known to occur along the MNAF. We finally explore the implications of several plausible scenarios to explain past slip history at the scale of the NAF system east of the Marmara Sea.

2 Geological context: the NAF in the Marmara region

The formation of the NAF initiated some 11-13 Ma ago within a wider pre-existing shear zone which progressively localized through time (Sengör et al., 2005, 2014). Starting possibly from eastern Anatolia, the fault zone grew by westward propagation through the lithosphere over ~10 Ma and reached the northern Aegean between 5 and 1 Ma ago (Armijo et al., 1996, 1999; Barka, 1992). From the Messinian and during the Pliocene, the NAF has functioned as a narrow zone, cutting through and deforming several basins inherited from the previous tectonic stages (Barka, 1992; Yılmaz et al., 1995). While the deformation is localized in a narrow zone in the eastern and central part of the NAF, it is structured on a wider area west of Düzce with a distribution of the deformation across several strands (Armijo et al., 1999; Fig. 1). The NAF strands show oblique kinematics, with local complex partitioning of the

deformation between dextral strike-slip and extensional regimes (Koçyigit & Özacar, 2003). The main northern strand (NNAF) continues along the strike of the main fault zone and crosses the northern part of the Marmara Sea from the Gulf of Izmit to Gelibolu Peninsula (Fig. 1). West of Akyazi district, another fault zone branches off from the NNAF, bounds to the south two successive basins known as the Geyve-Pamukova Basin and Iznik Lake, and reaches the south of the Marmara Sea through the Gulf of Gemlik as a single strand, which we term the middle strand of the NAF (MNAF) (Fig. 3a). West of Gemlik, this fault zone diffuses to a wider region (Sengör & Zabci, 2019; Sengör et al., 2005). Between the Gemlik Gulf and the Kapidag peninsula, the active deformation seems to distribute across two parallel fault strands. While the MNAF continues along the southern shore of Marmara, a southern fault strand (SNAF) continues west-southwestwards to Ulubat and Manyas Lakes (Fig. 1b). Further west, the deformation becomes more diffuse with highly distributed faulting, so that it is no longer possible to distinguish independent MNAF and SNAF strands among this southern NAF zone.

The MNAF has been traditionally divided into three major sections over a total length of 135 km (Barka and Kadinsky-Cade, 1988; Fig. 3). (1) Between the Gulf of Gemlik and Iznik Lake, the fault shows a roughly E-W direction (segment A), until a 12 km long releasing bend around Sölöz delta, southwest of the Lake. (2) The fault follows the southern coast of Iznik Lake with an E-W orientation (segment C), and continues in the narrow valley of the Kirandere with a constant azimuth of ~80°. This section in the west of Iznik Lake is marked by greater structural complexity and distribution of the deformation across several overlapping faults (segments D and E). Öztürk et al. (2009) suggested the existence of a continuous strike-slip fault extending along the deepest area of Iznik Lake, while Gastineau et al. (2021) evidenced an active fault strand following the northeastern edge of the lake's southern sub-basin, in a pull-apart configuration (Fig. 3b). East of Iznik Lake, Sipahioglu and

Matsuda (1986) reported the presence of two lineaments in this section: a geological boundary fault with no marker of Quaternary activation, and an active fault strand crosscutting and deforming recent alluvium. The eastern end of this section around the town of Mekece consists in a narrow, 1 km wide releasing step-over. (3) East of the step-over, the MNAF borders the south of the Geyve-Pamukova basin with a 70-80°N strike (segments F and G). The fault is associated to another fluvial system with the Sakarya River, collecting waters from the Anatolian plateau to the Black Sea. The river itself presents a large-scale right-lateral offset across the fault, estimated around 15-20 km (Fig. 3; Koçyigit, 1988; Özalp et al., 2013). The eastern edge of the basin is marked by a short restraining bend, after which the fault continues with a similar strike in the mountainous area of Akyazi where it connects to the main NAF (segment H).

3 Previous slip rates and paleoseismological studies on the MNAF

Geodetical horizontal slip rates along the MNAF of ~5±2 mm/yr were derived from strain accumulation modeling of fault-perpendicular GPS measurement profiles, despite a poor spatial distribution of the GPS sites (Ergintav et al., 2014; Straub et al., 1997). Meade et al. (2002) reported a similar estimate of 4.9±2.0 mm/yr for the segments east of Iznik using a GPS-based block modeling study. A more recent block modeling study estimated slip rates decreasing westward, and ranging between 4.2±1.3 mm/yr close to the MNAF-NAF junction and 3.1±1.5 mm/yr north of Manyas Lake (Fig. 2; Özbey et al., 2021). By comparison, the geodetic slip rate estimates along the NNAF in the Marmara region range at 20-25 mm/yr, with a lower horizontal rate of ~15 mm/yr in the Cinarcik basin south of Istanbul (Zabci, 2019).

The geological slip rates measured along the NNAF show lower values ranging at 15-20

mm/yr for the last 20 ka (Zabci, 2019). On the MNAF, a long-term horizontal slip rate was estimated by Gasperini et al. (2011) who used the displaced edge of a 11,250 years old submerged delta in Gemlik Bay to derive a 3.7±0.7 mm/yr minimal rate (Fig. 1b). This value was disputed by Vardar et al. (2014) who relied on a different offset value and an age of 30,000 years and derived a slip rate on the order of 2 mm/yr. Another value of 4.9±0.4 mm/yr was derived from the 16±1 km long offset of the Sakarya river in the Pamukova plain since the Late Pliocene (Özalp et al., 2013). The vertical motion was documented by Ikeda et al. (1991) who estimated a 0.7-1.4 mm/yr minimal rate from tilted post-glacial beachridges located on the western shore of Iznik Lake.

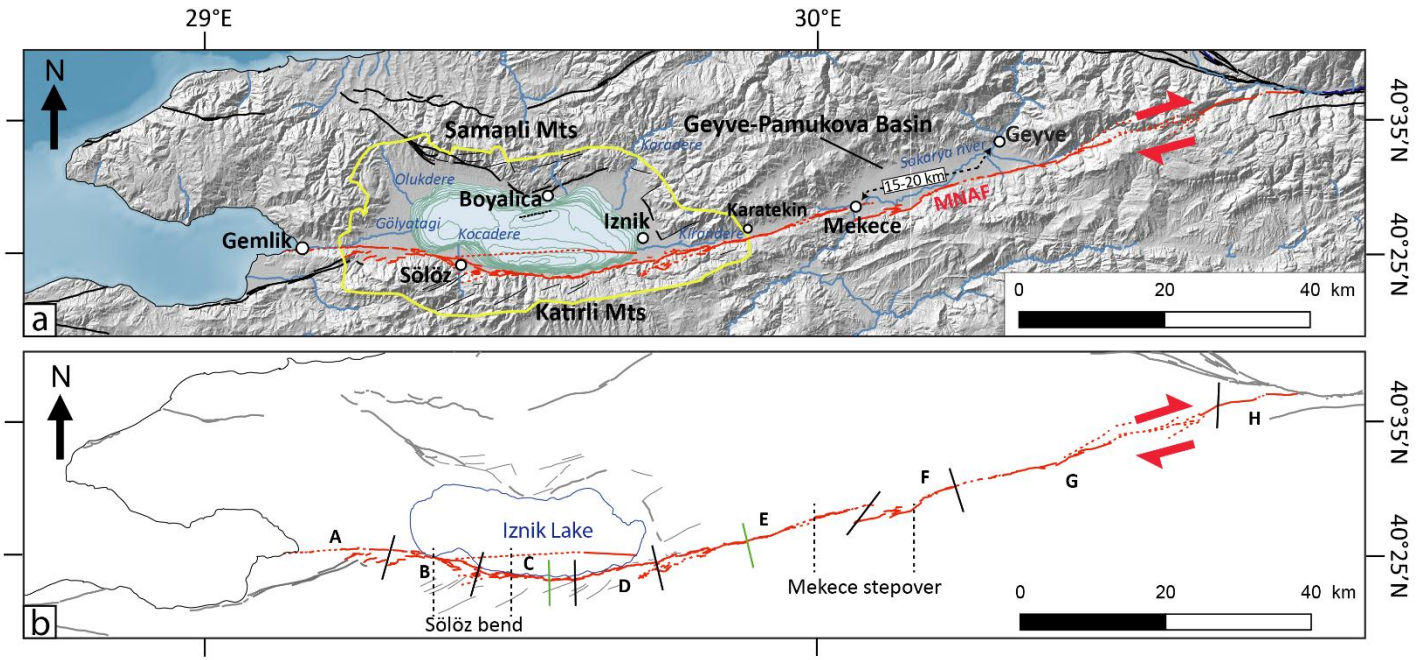

Figure 3. (a) General morphology of the eastern MNAF region. The footprint of the orthorectified Pleiades images (yellow) is superimposed on the Shuttle Radar Topography Mission (SRTM) model. The main rivers are drawn in blue. The MNAF is represented in red and the other active faults in black. Dotted lines indicate low confidence fault mapping (see section 4.2). The contours on the Iznik lake bottom are at a 5-meter interval (see Data Availability section). The fault traces within Iznik Lake are taken from Gastineau et al. (2021). (b) Segmentation of the main fault section analyzed in this study. Determined intersegments are located with black lines and alternative intersegments C/D et D/E with green lines (see section 4.3). Sölöz and Mekece step-overs' extent is shown with dashed lines.

A significant number of paleoseismological trenches have been dug along the MNAF (see e.g. the syntheses of Akyuz & Zabci, 2012; Fraser et al., 2010) that led to the identification of several ruptures during the last 4000 years (Fig. 2c). Yoshioka and Kusçu (1994) studied a site near Geyve and identified a 3rd century BCE rupture and a later undated one. In the same area, an unpublished trenching work by Akyüz et al. (2014) led to the identification of three presumed earthquakes. In the east of Iznik, the last rupture was dated between the 13-14th and 18th centuries CE (Honkura & Isikara, 1991; Ikeda, 1988). On the same segment, Barka (1993) opened nine trenches and found three ruptures since ~2000 BCE, but none of them were dated precisely. In the eastern part of Iznik Lake, Gastineau et al. (2021) evidenced a historical event in sediment cores, that they correlated to the 1065 CE earthquake. South of the lake, Erginal et al. (2021) reported a 50 cm high coseismic scarplet in beachrock deposits that they attributed to an 8th century rupture. On the same segment, Civico et al. (2021) opened two trenches and evidenced one mid-19th century event, one penultimate event after the late 7th century and two older events before the mid-5th century CE. West of Iznik Lake, Ikeda et al. (1989) proposed a mid-19th century event from archaeological remains found in a natural fault exposure. In Gemlik, Özalp et al. (2013) found a similar age for the last event and dated the penultimate between the 12th and 18th centuries. So far, the largest trenching work has been conducted by Dogan (2010) who opened 11 trenches on various MNAF segments. In many cases, very few or no age data could be retrieved, which makes it difficult to discuss whether the identified ruptures are independent from each other. Thus, in terms of earthquake recurrence, the paleoseismological data along the MNAF remain largely inconclusive due to partial results or occasionally contradictory findings (Fig. 2c).

4 Fault geometry and segmentation analysis

4.1 Imagery datasets used

Four stereo-pairs of Pleiades images covering the area between the Gulf of Gemlik, Iznik Lake, and Karatekin (Fig. 3a) were processed to obtain a high-resolution DEM using the NASA Ames Stereo Pipeline (ASP) software (Broxton and Edwards, 2008; Moratto et al., 2010; Shean et al., 2016) without using ground control points (Fig. 4c,d). The original Pleiades images have a resolution of about 50 cm, while the derived DEM has a horizontal resolution of 2 m and an absolute vertical precision better than 10 m. The DEM was then used to orthorectify the original optical images with the same ASP software. For the area east of 29.88E, which was not covered by our Pleiades images, we relied on Google Earth images (Pleiades images from CNES/Airbus, and QuickBird and WorldView images from Maxar Technologies), the SRTM elevation model and the active fault map of Emre et al. (2011).

4.2 Fault mapping and along-strike geomorphology

The trace of the MNAF between Karsak pass and Akyazi was mapped using the satellite imagery described in the previous section and complementary observations gathered in the field (Fig. 2a, 4). In the area benefiting from Pleiades coverage, secondary faults north and east of Iznik Lake were also mapped (Fig. 3). To locate the fault trace, we especially relied on high confidence geomorphological features, such as series of horizontally offset gullies and ridges, shutter ridges, well-defined scarps and facets. Along some other sections, particularly those lacking multiple consistent offsets, the mapping relied on lower confidence features, including large scale lineaments and slope breaks (Fig. 4).

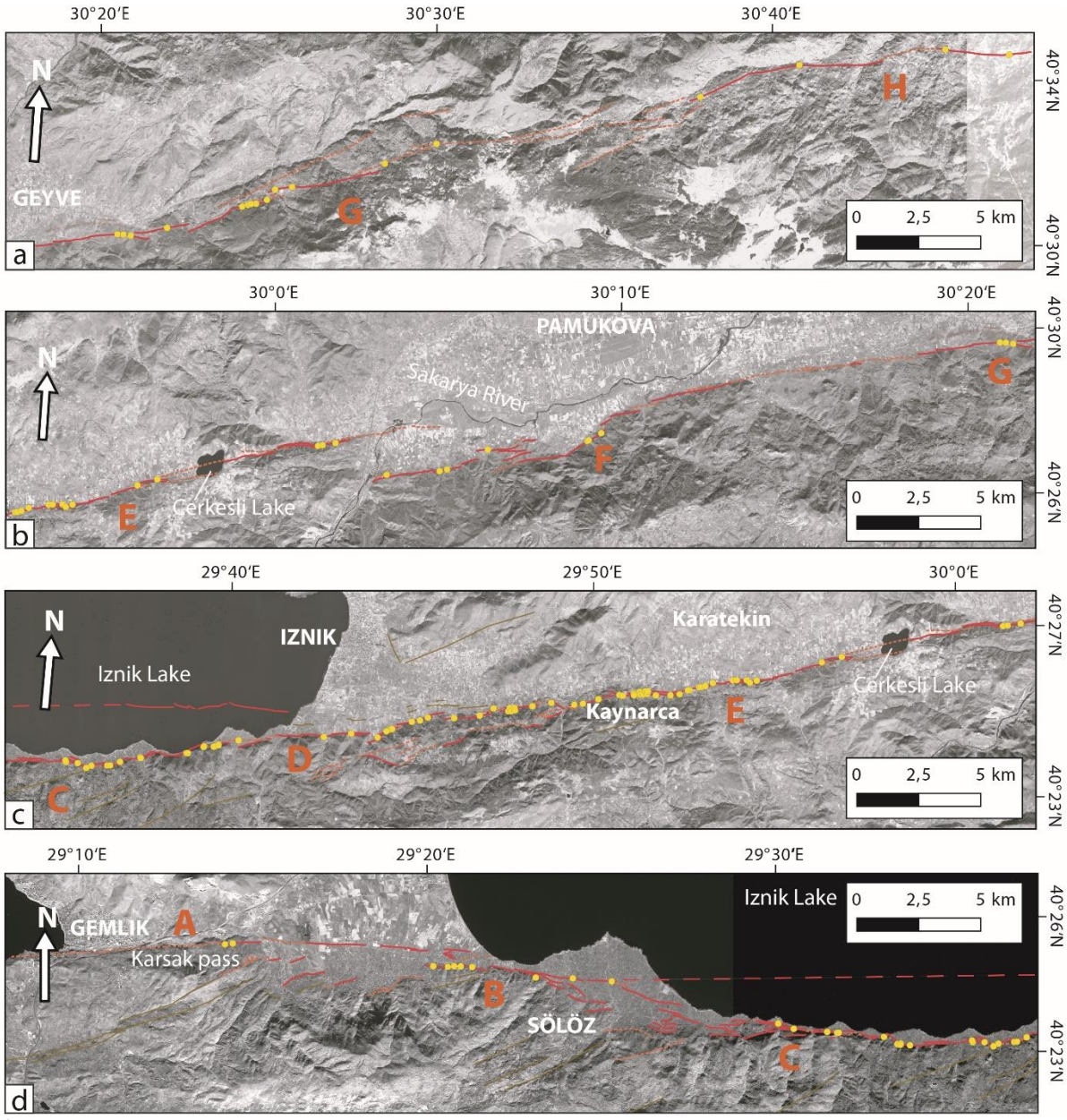

Figure 4. Surface trace of the eastern MNAF, superimposed on the Pleiades orthorectified images around Iznik Lake and Sentinel 2 images (Copernicus Sentinel Data [2018]) in other areas. Solid thick, dotted, and thin red lines refer to high confidence, low confidence, and secondary fault mapping, respectively. Other active faults are drawn in green. The subaqueous fault trace is taken from Gastineau et al. (2021). The yellow dots locate the markers associated with the offsets measured. The areas (a to d) are presented from east to west. Our proposed

segmentation (A to H) is also displayed.

Evidence for late Quaternary deformation can be observed in the landscape along the MNAF segments between the Gulf of Gemlik and Akyazi district (Fig. 2a, 3, 4). East of the Gulf of Gemlik, a small, E-W trending fault scarp borders the south of Gemlik alluvial plain and runs along the narrow Karsak pass (Fig. 4d). East of Karsak pass, several parallel faults stretch between the Eocene sedimentary rocks of the mountain range and the derived wide alluvial fan south of the Gölyatagi stream (Fig. 3a, 4d). Southwest of Iznik Lake, a set of overlapping and en echelon fault scarps are visible between the basement rocks and the Holocene alluvium of the large Sölöz delta, striking WNW-ESE. However, the horizontally offset markers are found along an E-W fault strand crossing the delta and forming a releasing bend with the fault section running south of the lake.

East of the delta, the fault shows again an E-W orientation with a succession of short, en echelon, recent scarps in the narrow coastal plain south of the lake (Fig. 4c, d). The association of several laterally offset gullies and vertical, south-facing scarplets (Fig. S1 and S2c) evidences the recent dextral motion across the fault with a normal component. A series of significant triangular facets have developed in the same section along the north-facing side of the Katirli range (Fig. 3a), which suggests long-term cumulative normal deformation in addition to the strike-slip tectonics. Southeast of the lake, the fault becomes more oblique to the main NAF direction, striking 80-85°N (Fig. 4c). East of Iznik Lake, the fault follows the southern edge of a 15 km long narrow, linear valley with a more continuous, simpler and straight trace (Fig. 4c). Between Iznik and Kaynarca, large-scale lineaments mark an oblique branch extending south of the main fault zone and striking 70°N. On the main fault line, markers of strike-slip deformation, such as shutter ridges, offset drainages and alluvial fan surfaces, are well developed (Fig. S2b). Occasionally,

parallel or en echelon successive faults can be traced in the landscape. This is the case between Kaynarca and Karatekin where secondary branching can be traced through a series of fan surfaces showing several offsets (Fig. 4c). This geometrical complexity is associated with an orientation change to 80°N. Close to Mekece, a series of laterally displaced streams running along a north facing scarp show cumulative dextral offsets ranging between 10 m and 25 m.

Further east, the fault crosses the Sakarya river and forms a ~1 km wide releasing step-over (Fig. 4b). The eastern section of the stepover is composed of shorter, en echelon faults. The fault then follows the southern edge of the Geyve-Pamukova basin as a single, simple straight trace with a 70-80°N, but is associated with fewer markers of Holocene horizontal deformation. East of the Geyve plain, the fault runs in the middle of a mountainous area and the precise mapping of the junction with the main NAF strand is less certain (Fig. 4a).

4.3 Fault segmentation

To properly interpret the set of deformed markers observed along the fault, it is needed to first determine the fault segmentation. Such segmentation can also provide first-order constraints on the maximum length and magnitude of earthquake that can be expected. The kind of boundary between the successive segments (azimuth difference, width and length of the step-overs. . .) is also thought to control whether a given rupture is likely to propagate through several segments (Aki, 1984; Barka & Kadinsky-Cade, 1988; Wesnousky, 2006). We decomposed the eastern MNAF zone into several successive segments using the automatic procedure developed by Klinger (2010). The digitized MNAF trace was first simplified and resampled each 50 m. The numerical method models the fault as a continuous set of linear segments and seeks, for a given

number of segments, the distributions of segment boundaries which best approximate the actual fault trace, using a l_1 trend filtering method (Kim et al., 2009). The brutal increase in the curve of the RMS-misfit as a function of the number of segments indicates that a minimal range between 8 and 19 segments is needed to describe the fault trace with a good trade-off between data-model misfit and limited number of segments (Fig. S3). We especially explored this space of solutions and found that the locations of most frequently selected inter-segments for this range cluster on 12 points of the fault. Keeping the solutions that included the most visible geometrical discontinuities along strike (e.g. Sölöz and Mekece stepovers, kinks at 29°35'E and south of Iznik) led us to favor a decomposition of the MNAF into 8 segments (denoted A to H on Fig. 3b).

Overall, the boundaries most frequently selected correspond to the major strike change occurring south of Iznik Lake (C/D inter-segment, Fig. 3b) and the releasing bend at the eastern edge of the Geyve-Pamukova basin (G-H inter-segment). The significant discontinuities of Sölöz bend (B/C inter-segment) and Mekece stepover (E/F inter-segment) also correspond to recurrently selected boundaries. Some other chosen boundaries are less recurrent. The D/E inter-segment is associated with a minor variation in azimuth but also with a more visible change from multiple parallel branches to a single, simpler fault trace eastward. The F/G inter-segment also reflects a transition from small en echelon faults to a single linear fault line eastward.

5 Cumulative and coseismic offsets

5.1 Method of measurement and uncertainties

Major ground rupturing earthquakes generate meter-scale deformations that can be preserved in the morphology through several seismic cycles (e. g. Ansberque et al., 2016; Klinger et al., 2011; Kurtz et al., 2018). In the case of strike-slip ruptures, it is generally possible to measure in the days following the earthquake a series of laterally displaced markers such as roads, fences, walls, field or vegetation lines, terrace risers or gullies (Rockwell et al., 2002). Older morphological markers can also show larger, cumulative values of offset representing the summation of several coseismic displacements. If enough markers of various ages are preserved along the fault, the compilation of a large number of offset measurements is expected to give several clusters of values, corresponding to the cumulative displacement for various numbers of earthquakes (Beauprêtre et al., 2012, 2013). The offset measurements carried out after recent earthquakes have evidenced that the coseismic slip located on the fault often shows significant variations along-strike, as high as 30-40% around the mean displacement (Choi et al., 2018; Lin et al., 2020; Reitman et al., 2019; Rockwell et al., 2002; Zielke, 2018). The off-fault deformation, which is difficult to measure during post-seismic surveys, can also be significant (Antoine et al., 2021; Choi et al., 2018; Rockwell et al., 2002). Despite the erosive and sedimentary processes which tend to erase the smallest coseismic offsets, the measurement of cumulative offsets can also give access to this slip variability on longer time scales (Rizza et al., 2011).

	Total	Segment A	Segment B	Segment C	Segment D	Segment E	Segment F	Segment G	Segment H
Length (full mapping, km)	148	14.4	12.5	13.9	11.5	31.2	16.4	36.6	11.5
Length (confident mapping, km)	107	4.1	12.5	13.6	11.1	24.1	14.9	17.3	9.2
Number of measurements	114	2	10	14	15	50	7	12	4
Measured on Pleiades topography	45	1	6	8	8	22	0	0	0
% Pleiades topography	39	50	60	57	53	44	0	0	0
Measured on Pleiades image	32	1	4	6	7	14	0	0	0
% Pleiades image	28	50	40	43	47	28	0	0	0
Measured on Google Earth image	37	0	0	0	0	14	7	12	4
% Google Earth image	32	0	0	0	0	28	100	100	100
Mean quality /20	12	14	12	11.1	12.3	12.3	10.7	11.8	12.3
Density of data per km	0.77	0.14	0.80	1.01	1.30	1.60	0.43	0.33	0.35
Density of data (confident mapping)	1.07	0.49	0.80	1.03	1.35	2.07	0.47	0.69	0.43
Number of COPD peaks (2σ model)			5	7	11	8	4	6	
Number of COPD peaks (1σ model)			4	4	5	8	4	4	2

Table 1. Summary of the main characteristics of the fault mapping and offset measurements datasets used in this study.

Along a 148-km long portion of the eastern MNAF, we identified and systematically measured 114 offsets (Tables 1 and S3, see Data Availability section). 40% of the measurements were performed using Pleiades topographic data, while Pleiades ortho-rectified images and Google Earth images each represent 30% of the measurements. The displaced markers considered are river channels, gullies, terrace risers and more occasionally vegetation lines and ridges. We favored markers making a high angle with the fault in order to minimize the apparent offset linked to unaccounted-for vertical slip. For each marker, we define piercing lines, i.e. points that were aligned before the displacement, and that we project on the fault trace. The piercing points across the fault are then realigned by retro-deformation, which gives the offset value (Fig. 5). When one marker is displaced by several parallel fault strands, the offset value to be considered is the sum of the measurements on each fault line (Zielke et al., 2015). Five offsets were also measured in the field with tape (Fig. 6). One field measurement (marker 153) ranges significantly lower than the Pleiades measurement due to different reconstruction hypothesis. The other field measurements are in general in fair agreement with the values obtained from satellite imagery, though ~10% lower on average. The relative underestimation of field offset measurements compared to satellite imagery has been noticed in previous studies (see another example in Klinger et al., 2005) suggesting that the distributed deformation is better assessed in the latter case (Antoine et al., 2021).

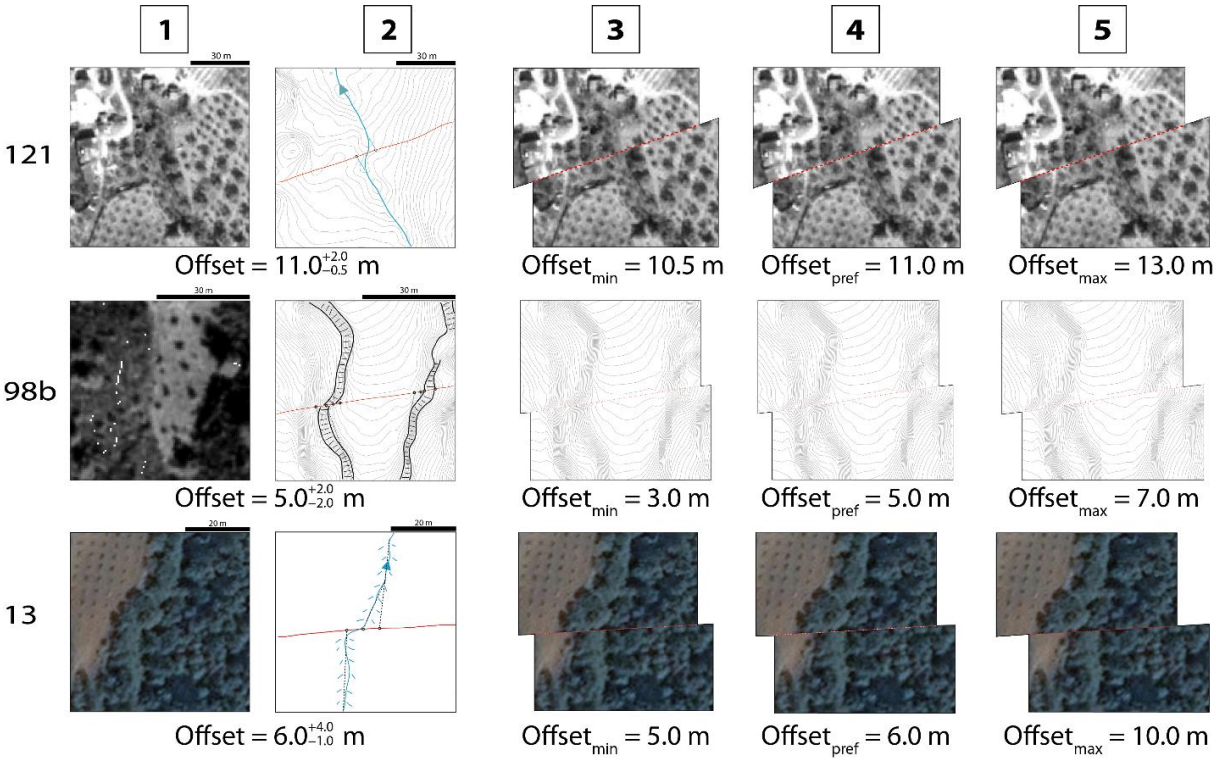

Figure 5. Examples of horizontal offset measurements. Marker ID code is indicated on the left. North direction is upward. From top to bottom, measurements were respectively done using the Pleiades image, topography, and the Google Earth image. Columns 1 and 2 show the original morphologies. The fault is drawn in red. Black lines and circles refer to the piercing lines and points. Columns 3, 4 and 5 show the retro-deformed morphologies giving the minimum, preferred and maximum offset values respectively. For the full dataset, see Data Availability section.

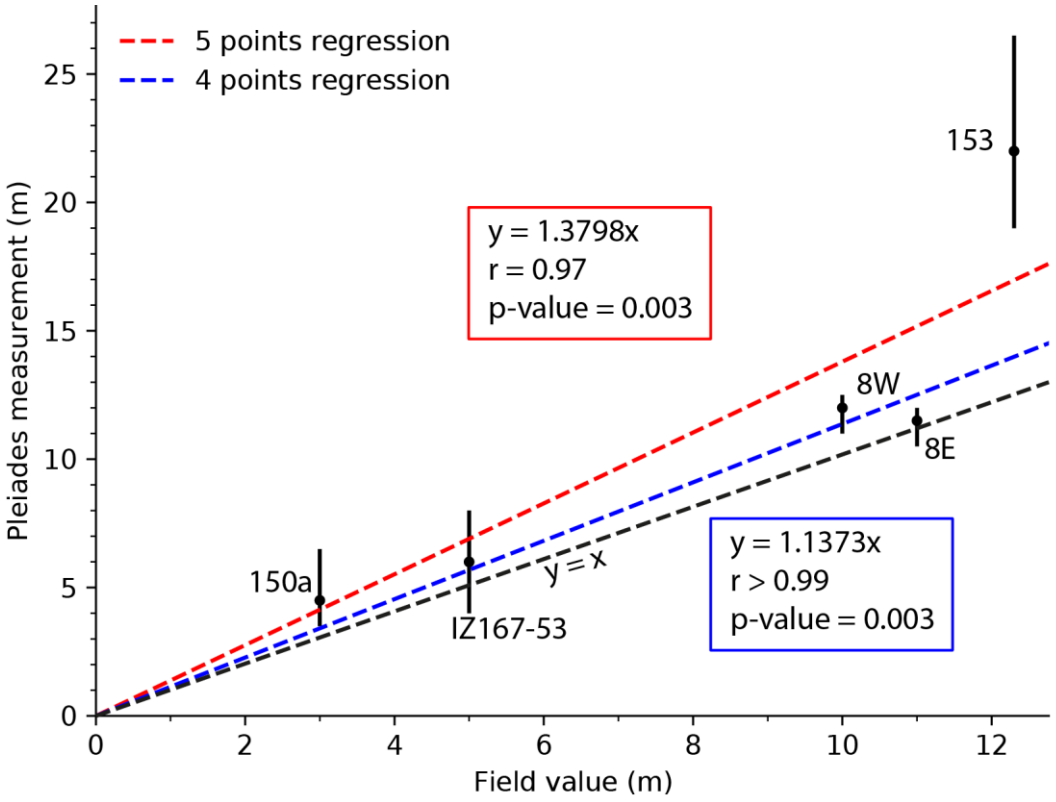

Figure 6. Comparison between field and Pleiades offset measurements. Two linear regressions are shown, including all data points (red) and excluding marker 153 (blue). For each regression we present the equation, Pearson's correlation coefficient *r* and the p-value.

The uncertainty of the offset measurement mainly originates from the various possibilities for interpreting and restoring the original, non-deformed geometry of the marker (Ansberque et al., 2016; Manighetti et al., 2015). Therefore, each measurement consists in our preferred value for the best reconstruction, and a minimum and a maximum value, each representing an extreme plausible reconstruction. We use conservative min/max reconstructions, larger than ±15% of the preferred value on average, so that there is only a small probability that the real offset falls out of this range (Gold et al., 2013). Each measurement is given a 20-points quality score, which reflects the intrinsic quality of each marker in providing a relevant measure (Beauprêtre et al., 2013; Choi et al., 2018; Kurtz et al., 2018; Zielke et al., 2012).

This score includes the following criteria: (a) confidence that the offset marker is of tectonic nature and weakly man-modified, (b) degree of preservation (marker visibility and sharpness), (c) marker shape (width and sinuosity), (d) fault zone complexity (plausible fault zone width and number of fault splays), (e) angle of marker with fault, (f) resolution of used dataset (a detailed explanation of how the quality score is determined can be found in Supporting Information).

5.2 Statistical analysis

The 114 offsets measured range between 2.5 and 64 m, with a majority of values smaller than 30 m (Fig. 7b, Table S3). In order to identify the most significant offset clusters along each fault segment, which could represent the cumulative signature of past ruptures, we represent the offset values as probability density functions (e.g. Beauprêtre et al., 2012; Kurtz et al., 2018; McGill and Sieh, 1991; Zielke et al., 2010). Each offset measurement is represented with an asymmetric Gaussian distribution, the preferred measured value being the peak of the Gaussian probability density function (PDF). Since the minimum and maximum offsets reflect geologically plausible bounds for the reconstruction values and do not directly correspond to real standard variations (Scharer et al., 2014), we compare two models where these maximum and minimum ranges are taken as $\pm 1\sigma$ and $\pm 2\sigma$ half-widths of the PDF (referred hereafter as "1σ model" and "2σ model").

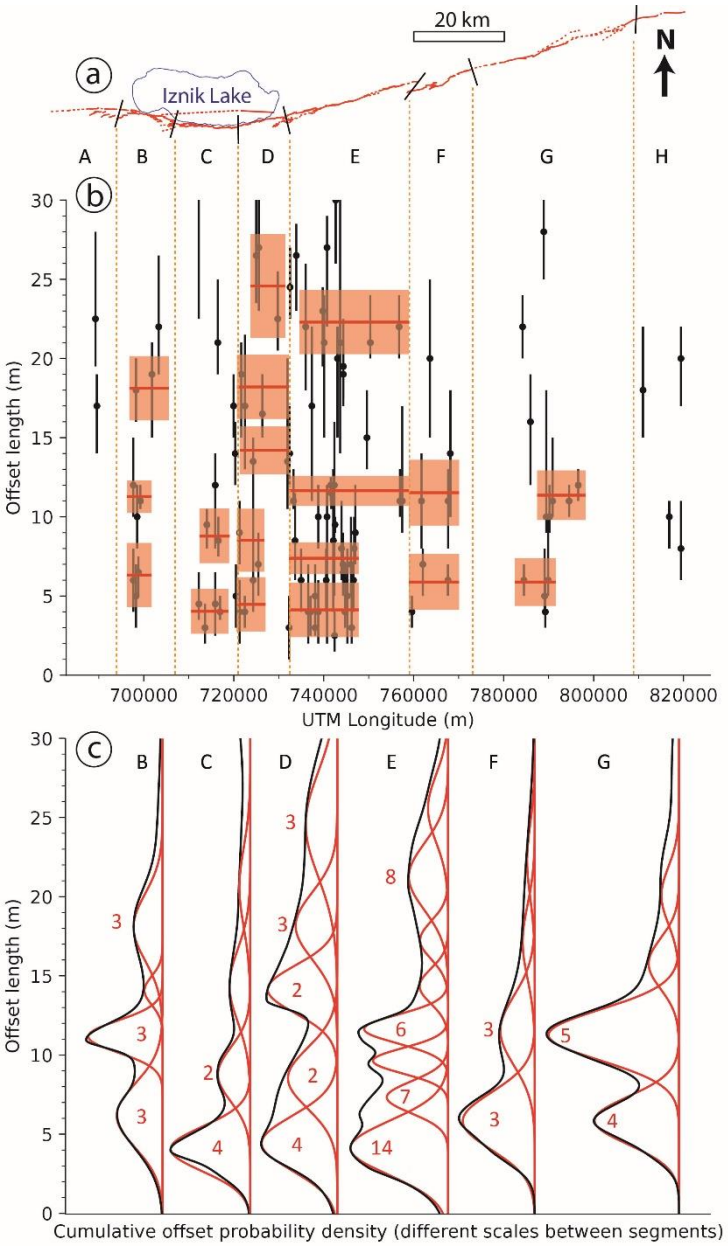

Figure 7. (a) Map of the fault section studied with our proposed segmentation. (b) Horizontal offsets measured along the fault in the range 0-30 m. The color boxes represent the best constrained peak values, within 1σ uncertainties, obtained on the cumulative offset probability distribution (COPD) curves for each segment. The segments are separated by the vertical orange broken lines. (c) COPD curves (black lines) and modeled average slips (red lines) for the 1σ model. The number of supporting individual measurements is indicated for the best constrained COPD peaks.

The individual PDFs for each segment are then summed into a cumulative offset probability distribution (COPD) curve, using the quality scores as weights for each individual offset measurement (Fig. 7c and 8a). The COPD generally presents local peak values, which indicate the most frequent offsets measured along the fault section considered. The contribution of each measurement in the shape of the COPD depends both on its uncertainty and on its quality score. A larger uncertainty corresponds to a wider and flatter individual PDF, which consequently contributes less to define a clear COPD peak. A lower quality score decreases the effect of the measurement in changing the shape of the COPD. For each COPD curve, it is assumed that the value associated to the first peak value corresponds to the offset related to the most recent large earthquake preserved along that specific segment. The average slip associated with this last rupture is empirically extracted from the COPD through several steps (Kurtz et al., 2018). (1) The rising part of the COPD curve is used to build a symmetric Gaussian function, which represents the modeled average slip associated to the most recent rupture along the segment considered. (2) This modeled function is subtracted from the COPD to derive a residual COPD (Fig. 8b). This residual curve is assumed to represent the cumulative tectonic deformation recorded in the landscape before the most recent earthquake occurred. (3) In general, the rising part of the COPD does not strictly follow a Gaussian function, which produces a residual negative artefact located ahead of the following peak values. This residual is discarded by resetting all negative values to zero before the next extraction. As these steps are iterated (Fig. 8c), the residual COPD curve flattens and the Gaussian fit becomes less constrained. To avoid extracting artifacts which are not supported by measurements, the peaks with an amplitude below 10% of the maximum amplitude of the original COPD are judged unreliable and are discarded (following Kurtz et al., 2018). The iterations are stopped when no additional peak can be

constrained.

The validity of this method for extracting peaks and interpreting them as slip signals relies on several assumptions. The resolution of satellite imagery and the uncertainties of offset measurements limit the detection of small slip signals. In our case, this minimum detectable slip ranges at ~2.5 m, which implies we cannot detect events of Mw below 7. We assume that the variability of coseismic slip over short distances along strike is limited enough to produce relevant clusters of offset measurements. It is also assumed that these measurements result from predominantly intermittent and seismogenic slip with negligible contributions of creep, slow slip or afterslip. The production of geomorphic markers must happen more frequently than the large earthquakes for the geomorphic slip record to be complete. The production of these markers is also assumed to be stable over the time window considered. These assumptions will be addressed together with the discussion of the results.

Interpreting COPD peaks as individual slip signals must be done with caution, especially when relative measurement uncertainties are high and when only few data points are available along a segment. Because of the natural variability in coseismic slip along strike, offset measurements from a single event can produce bimodal distributions (Lin et al., 2020; McGill & Rubin, 1999). Conversely, one large increment might hide two separate, smaller events, but undistinguished due to too few data and/or too large individual uncertainties (e. g. Liu-Zeng et al., 2006; Zielke et al., 2010). Once the COPD peaks are extracted for a given segment, we assess the statistical significance of each peak by looking at the following criteria (Tables 2 and 3): number of supporting individual measurements, spreading of the data supporting the first two peaks, degree of overlapping with preceding peak, sensitivity to alternative segmentation (for segments C, D, E).

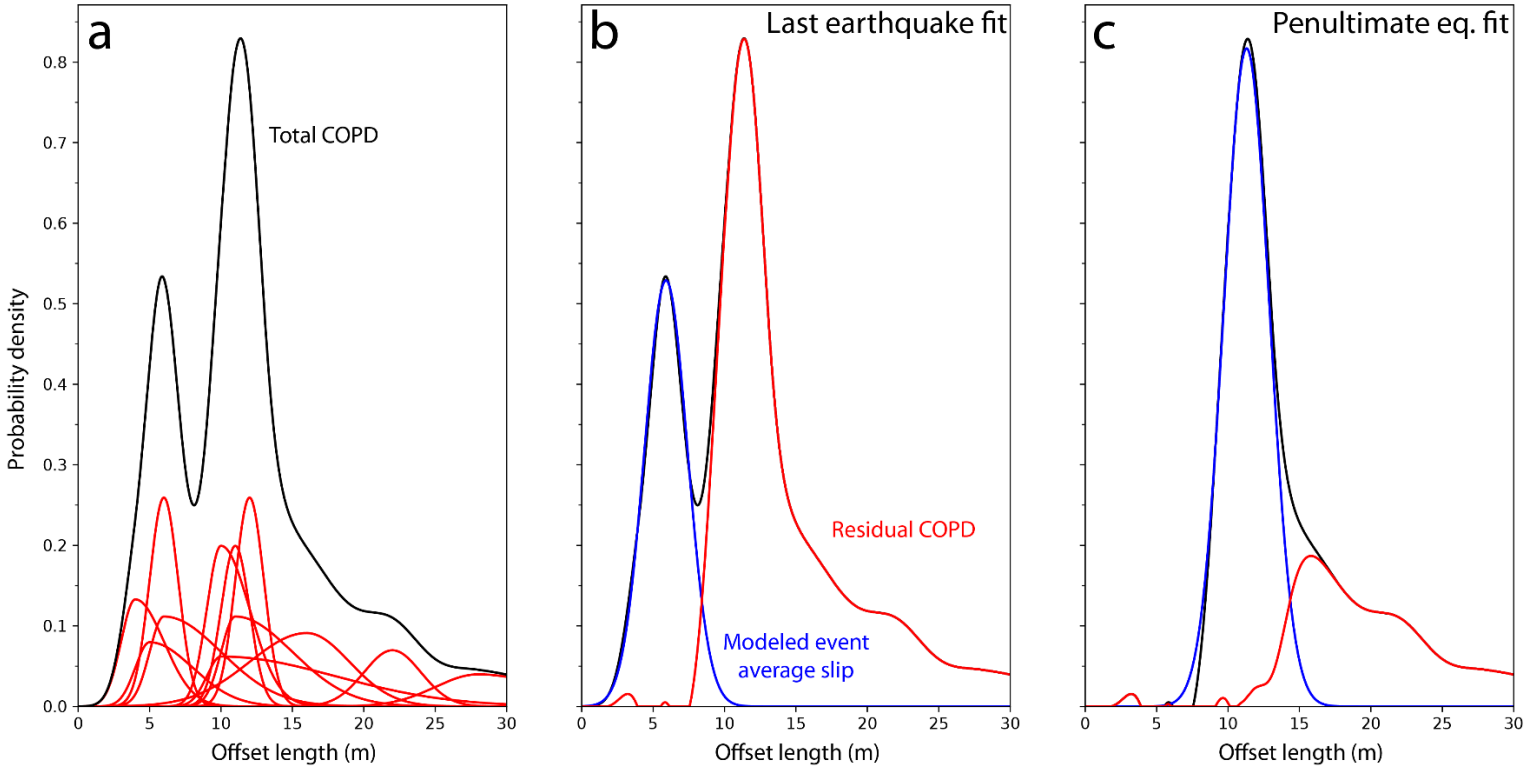

Figure 8. Illustration of the statistical analysis methodology used for the offset measurements of segment G. (a) Probability density functions of the individual measurements (in red) and corresponding Cumulative Offset Probability Density (COPD, in black). (b) Modeling of the last major surface rupture signal by fitting the increasing part of the COPD with a Gaussian curve (in blue). The red line is the residue of the COPD after subtracting this last rupture slip model. (c) Same process as (b) for the presumed penultimate event.

5.3 Results

Tables 2 and 3 present the offset values extracted from the COPD peaks for each fault segment in the range 0-30 m. We extracted between 4 and 11 peaks per segment for the 2σ model and between 4 and 8 peaks for the 1σ model (Table 1). Smaller modeled uncertainties tend to increase the number of extracted peaks per segment. This effect is most significant for segment D where the number of peaks for the 2σ model is two times larger. However, most of the extracted peaks for the 2σ model show poor statistical robustness. Half of them are not supported by more than one individual measurement (Table 3). For some of them, the increment with the preceding peak is not significantly different from zero. Several of them do not pass the segmentation test. This likely results from a high degree of data scattering compared to uncertainties, especially for segments with small numbers of measurements. Segment E does not show this feature because of its high spatial density of measurements, which is more than twice as high as the average density of the other segments (Table 1).

To check for potential biases resulting from this higher density of measurements, we performed a supplementary test on segment E. We produced and analyzed five random subsets of 18 measurements obtained on segment E, so that the measurement density of the subsets equals the average density of the other segments, i.e. 0.75 measurement per km. We then identified which extracted peaks remained consistent between all subsets. The sensitivity tests for that segment suggest that only the first two peaks are statistically robust. These peaks still present a high degree of overlapping.

Most peaks obtained with the 1σ model are statistically stronger than those obtained with the 2σ model (Table 2). When only the more robust peaks are considered, both models show similar

287 results (Table 4, Fig. 7b). Segments A and H did not provide statistically significant peaks due to
288 the very small number of measurements.

289 We identified two to five statistically robust cumulative slip increments for segments B to G,
290 ranging between 4 and 25 m. Offset values show consistency between all segments for the first
291 two extracted peaks at ~5 and ~10 m. However, the central segments C, D and E show lower
292 mean values of increments, from 3.2 m to 4.7 m, while they range between 5 and 6.2 m on
293 segments B, F and G. On segment E, despite the higher density of measurements, the events are
294 harder to separate and their respective displacement is less constrained due to the larger
295 scattering of data points. Peak values differ more for higher peaks (Table 4).

Segment	Mean value	(±1σ)	Increment with preceding peak	(±1σ)	Number of supporting measurements	Mean quality	Spreading with previous peak	Overlapping coefficient with previous peak	Sensitivity to segmentation	Sensitivity to downsampling
B	6.2	2			3	12.7				
B	11.2	1	5	3	3	12	<30%	0.09		
B	14.1	0.9	2.9	1.9	0			0.13		
B	18.1	2.1	4	3	3	12		0.16		
C	4.1	1.4			4	14.3				
C	8.8	1.7	4.7	3.1	2	11	<30%	0.13		
C	14.4	2.3	5.6	4	3	9		0.16	x	
C	20.6	2.5	6.2	4.8	1	11		0.2		
D	4.5	1.7			4	12.3				
D	8.6	1.9	4.1	3.6	2	10	<30%	0.25		
D	14.2	1.5	5.6	3.4	2	14.5		0.1		
D	18.2	2.1	4	3.6	3	14		0.26		
D	24.6	3.3	6.4	5.4	3	11.3		0.23		
E	4.2	1.7			14	12.8				
E	7.4	1	3.2	2.7	7	12.1	<30%	0.23		
E	9.7	0.8	2.3	1.8	4	10.8		0.2		x
E	11.7	0.9	2	1.7	6	13.3		0.24		
E	14.4	1.1	2.7	2	2	11		0.18		x
E	17.3	1.2	2.9	2.3	2	13		0.21	x	x
E	21.3	2.1	4	3.3	8	11.6		0.21		
E	25.6	2.1	4.3	4.2	3	13.7		0.31	x	x
F	5.9	1.8			3	10.7				
F	11.6	2.2	5.7	4	3	10	<30%	0.15		
F	17.2	2.3	5.6	4.5	0			0.21		
F	22.3	2.3	5.1	4.6	1	13		0.27		
G	5.9	1.5			4	11.3				

G	11.3	1.6	5.4	3.1	5	13.2	<30%	0.08		
G	15.8	1.6	4.5	3.2	1	16		0.16		
G	20.1	1.8	4.3	3.4	1	7		0.21		
H	9.4	2			2	13				
H	18.7	2.7	9.3	4.7	2	11.5	30-40%	0.05		

296 **Table 2.** COPD peaks extracted for the 1σ model. Mean quality is computed on the set of individual measurements supporting each
297 peak. Spreading value is expressed in % of the mean of measurements supporting the first two peaks per segment. The overlapping
298 coefficient is computed using normalized distributions.

Segment	Mean value	(±1σ)	Increment with preceding peak	(±1σ)	Number of supporting measurements	Mean quality	Spreading with previous peak	Overlapping coefficient with previous peak	Sensitivity to segmentation	Sensitivity to downsampling
B	6.1	1.3			3	12.7				
B	9.9	0.6	3.8	1.9	1	13	<30%	0.04		
B	11.1	0.4	1.2	1	1	15		0.22		
B	12.3	0.9	1.2	1.3	1	8		0.32		
B	18.2	1.4	5.9	2.3	2	13.5		0.01		
C	3	0.5			1	17				
C	4.2	0.5	1.2	1	3	13.3	>40%	0.23		
C	5.4	0.5	1.2	1	0			0.23		
C	9	0.8	3.6	1.3	3	10	<30%	0.05		
C	13.9	1.6	4.9	2.4	1	11		0.04	x	
C	17.2	0.7	3.3	2.3	1	8		0.14	x	
C	21.2	1.6	4	2.3	1	11		0.07		
D	4.2	0.8			3	14				
D	6.8	1	2.6	1.8	2	6.5	30-40%	0.15		

D	9	1	2.2	2	1	14	<30%	0.27		
D	13.2	1.9	4.2	2.9	0			0.14	x	
D	13.7	0.5	0.5	2.4	2	14.5		0.42		
D	14.9	0.5	1.2	1	0			0.23		
D	16.6	0.7	1.7	1.2	2	15		0.15		
D	18.2	0.9	1.6	1.6	1	12		0.31	x	
D	19.8	0.6	1.6	1.5	1	12		0.26		
D	22.5	1.2	2.7	1.8	1	14		0.16	x	
D	26.5	1.7	4	2.9	2	10		0.16		
E	3.8	1			10	13				
E	6.4	0.9	2.6	1.9	7	11.3	<30%	0.17		
E	8.3	0.6	1.9	1.5	4	13.8		0.2		x
E	9.6	0.5	1.3	1.1	4	10.8		0.24		x
E	11.4	0.7	1.8	1.2	6	13.3		0.13	x	x
E	14.4	1.5	3	2.2	3	11.7		0.16	x	x
E	19.7	1.7	5.3	3.2	6	12.8		0.1		x
E	24	2.6	4.3	4.3	5	11.4		0.31	x	
F	4	0.5			1	9				
F	6.2	0.8	2.2	1.3	2	11.5	>40%	0.09		
F	11.1	1.5	4.9	2.3	3	10	<30%	0.03		
F	19.6	3	8.5	4.5	1	13		0.06		
G	4.1	0.6			2	9				
G	6	0.7	1.9	1.3	2	13.5	>40%	0.14		
G	8	0.5	2	1.2	0			0.09		
G	11.3	1.2	3.3	1.7	5	13.2	<30%	0.05		
G	15.2	1.2	3.9	2.4	1	16		0.1		
G	22	1.1	6.8	2.3	1	7		0.003		

299

Table 3. COPD peaks extracted for the 2σ model. Mean quality is computed on the set of individual measurements supporting each peak. Spreading value is expressed in % of the mean of measurements supporting the first two peaks per segment. The overlapping coefficient is computed using normalized distributions.

	COPD peak values (m)					Increments between peaks (m)				
	Peak 1	**Peak 2**	**Peak 3**	**Peak 4**	**Peak 5**	**Peak 1**	**Peak 2**	**Peak 3**	**Peak 4**	**Peak 5**
B	**6.2±2** (6.1±1.3)	**11.2±1.0**	**18.1±2.1** (18.2±1.4)			**6.2±2** (6.1±1.3)	**5±3.0**	**6.9±3.1** (12.1±2.6)		
C	**4.1±1.4** (4.2±0.5)	**8.8±1.7** (9.0±0.8)				**4.1±1.4** (4.2±0.5)	**4.7±3.1** (4.8±1.3)			
D	**4.5±1.7** (5.5±1.8)	**8.6±1.9**	**14.2±1.5** (13.7±0.5)	**18.2±2.1** (16.6±0.7)	**24.6±3.3** (26.5±1.7)	**4.5±1.7** (5.5±1.8)	**4.1±3.6**	**5.6±3.4** (8.2±2.3)	**4.0±3.6** (2.9±1.2)	**6.4±5.4** (9.9±2.4)
E	**4.2±1.7** (3.8±1.0)	**7.4±1.0** (6.4±0.9)	**11.7±0.9**	**22.3±2.1**		**4.2±1.7** (3.8±1.0)	**3.2±2.7** (2.6±1.9)	**4.3±1.9**	**10.6±3.0**	
F	**5.9±1.8** (5.1±1.3)	**11.6±2.2** (11.1±1.5)				**5.9±1.8** (5.1±1.3)	**5.7±4.0** (6.0±2.8)			
G	**5.9±1.5** (5.1±1.3)	**11.3±1.6** (11.3±1.2)				**5.9±1.5** (5.1±1.3)	**5.4±3.1** (6.2±2.5)			

Table 4. Best constrained cumulative offsets and slip increments computed for each fault segment in the offset range 0-30 m. The retained peaks respect the following conditions: significant increment with preceding peak, more than one supporting individual measurement, less than 30% of spreading with previous peak, consistency through varying segmentation and downsampling. Uncertainties are 1σ. Bold values are from the 1σ model. Values in brackets are those deduced from the 2σ model. We underline values showing consistency between the two models.

6 Terrace dating

Terrace	Sample code	Depth (cm)	Dissolved quartz mass (g)	^{9}Be carrier solution (g)	^{10}Be/^{9}Be ratio ± 1σ AMS uncertainty (10^{-15} blank corrected)	^{10}Be (10^{4} at/g)	^{10}Be concentration uncertainty (%)	Sampling site location
T3	15TUR5-0a	0	17.179	0.2988	9.913 ± 1.208	1.1499	23.05	40.3974°N - 29.6966°E
T3	15TUR5-0b	0	18.480	0.2990	23.17± 6.328	2.5003	34.99	94±4 m asl
T3	15TUR5-20	20-35	2.864	0.3010	3.428 ± 0.744	2.4060	69.82	TS = 0.997
T3	15TUR5-60	60-70	10.739	0.2995	8.012 ± 0.956	1.4902	25.69	
T3	15TUR5-80	80-90	16.347	0.2980	12.25 ± 1.234	1.4896	17.91	
T3	15TUR5-130	130-140	6.789	0.2976	3.808 ± 0.556	1.1132	49.12	
T2	15TUR3-0a	0	20.549	0.3043	178.5 ± 6.176	17.6296	3.65	40.4963°N - 29.6813°E
T2	15TUR3-0b	0	18.510	0.3078	89.09 ± 5.310	9.8809	6.52	127±3 m asl
T2	15TUR3-60	60-85	20.824	0.2989	53.09 ± 4.953	5.0837	10.65	TS ~ 1
T2	15TUR3-110	110-130	19.941	0.2905	245.1 ± 8.848	23.8183	3.75	
T2	15TUR3-150	150-175	17.038	0.2993	200.4 ± 32.61	23.4781	16.79	
T1	15TUR4-0a	0	20.838	0.2979	226.9 ± 75.69	21.6293	34.27	40.5031°N - 29.6860°E
T1	15TUR4-0b	0	20.514	0.2973	313.7 ± 11.86	30.3225	3.89	164±3 m asl
T1	15TUR4-30	30-40	20.550	0.2958	255.4 ± 7.943	24.5165	3.24	TS ~ 1
T1	15TUR4-80	80-90	23.547	0.2981	292.6 ± 11.47	24.7008	4.03	
T1	15TUR4-130	130-140	20.510	0.2984	326.3 ± 10.80	31.6621	3.41	
T1	15TUR4-260	260-270	22.204	0.2966	184.8 ± 9.776	16.4640	5.52	
T1	15TUR4-370	370-380	20.771	0.2980	243.5 ± 12.71	23.2995	5.38	

Table 5. Characteristics of the terrace samples and results of the nuclide measurements. The ^{10}Be/^{9}Be ratio of the blank is $6.200.10^{-15}$ with an analytical uncertainty of 19%. TS is topographic shielding value. The total measurement error includes the uncertainties associated with the AMS measurement, the blank value, the dissolved quartz mass and the spike mass weighing and concentration.

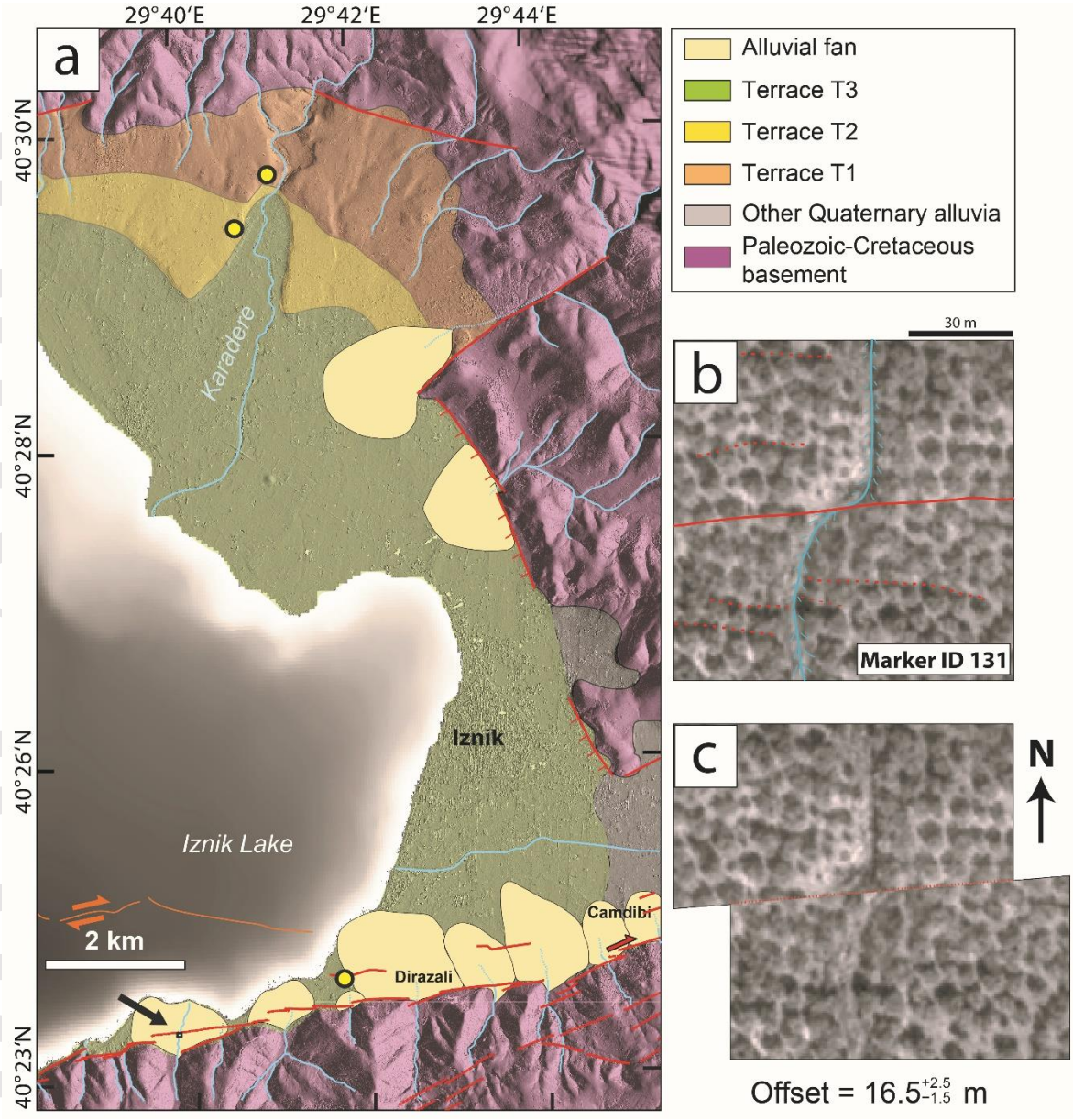

Figure 9. (a) General location of the terrace sampled for cosmogenic dating (yellow dots). Active faults are mapped in red-orange and main streams are drawn in blue. The subaqueous fault trace is taken from Gastineau et al. (2021). The eastern limit of terrace T3 is not well defined in the geomorphology and was drawn assuming a constant elevation. The marker used to derive a minimum horizontal slip rate is indicated with a black arrow. (b) Interpreted Pleiades image of the present-day marker morphology. (c) Preferred retro-deformed morphology.

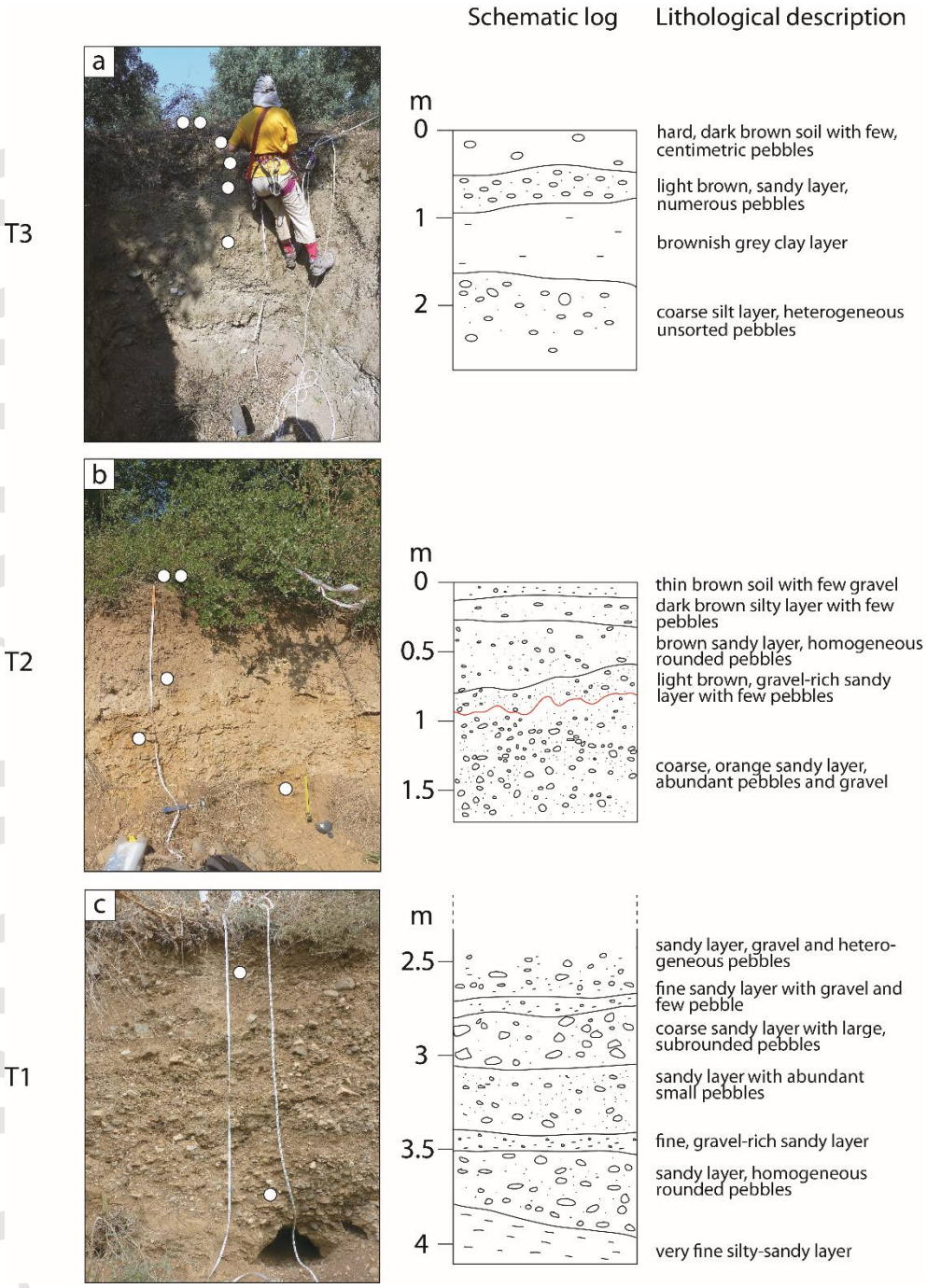

Figure 10. Field photographs (left) and interpreted stratigraphy (right) of the terrace profiles sampled for dating, T3 (a), T2 (b), and T1 (c). The samples are represented with white circles. The first meters of T1 profile were covered with bushes, and consisted of a homogeneous brown, silty-sandy unit with a few centimetric pebbles.

Actually, the statistical analysis of cumulative offsets evidences the occurrence of past ruptures along the MNAF and documents the associated slip-per-event, but does not inform the age of these events. To narrow down the age range for the identified events and estimate the late Quaternary slip rate of the MNAF, we need constraints on the age of the terranes that were offset by the fault. The area surrounding Iznik Lake displays low gradient alluvial fans emplaced on three preceding levels of abandoned lake plains, which were targeted in this study. These flat levels, separated by wave-cut scarps, have been known and interpreted as lacustrine terraces since the early 20th century (Chaput, 1936; Tanoglu and Erinc, 1956). They appear particularly well-developed north and east of Iznik Lake (Ikeda et al., 1991; Fig. 9a). The terraces were presumably deposited originally with a small slope, but the current slope tends to increase with elevation and age, and also in the central part as the terraces get closer to the mountain range. The lowest scarp associated with the youngest lake plain (Tl3) is the clearest and can be traced almost over the entire length of the northern coast. The height of its inner edge above the present lake level (a.l.l.) is about 20 meters northwest Boyalica village. The intermediate terraceT2 can also be easily traced in the west but is hardly visible in the central part around Boyalica. The associated wave-cut scarp appears again in the wider alluvial plain northeast of the lake, with an inner edge 60 m high a.l.l. The highest and oldest terraceT1 is much more degraded but can still be traced almost continuously in the west with a 110 m a.l.l. high inner edge. Remnants of this old paleoshoreline and the associated sediments can be observed in the northeast, especially along an irrigation canal constructed west of the Karadere stream. In the southern part, these successive terrace levels cannot be unambiguously mapped and have been partly overlain by younger alluvial sediments, especially in areas where the lake shore comes very near to the foot of the mountain front.

360 **6.1 Sampling and analytical method**

361 To date the terraces, we used the *in-situ* produced terrestrial cosmogenic nuclide (TCN) method.
362 The terraces were sampled along vertical profiles (Fig. 10, Table 5). For terraces T1 and T2,
363 samples were taken on pre-existing, man-made scarps. These scarps have been laterally refreshed
364 due the surrounding agricultural activity, preventing a significant nuclide accumulation from
365 posterior lateral exposure. For terrace T3, we benefited from a pit dug in the plain for
366 hydrological maintenance. The pit is located close to the western edge of the major fan of
367 Dirazali, so an alluvial contribution posterior to the emersion of the lake plain cannot be ruled
368 out. The outcrops displayed alternations of fine sand and coarser gravel-rich conglomerate with
369 graded bedding, with no evidence of buried paleosols. T1 and T3 mainly showed alluvial facies,
370 the former displaying evidence of paleochannels and cross-stratification. T2 showed lateral
371 facies variations, with finer, lacustrine deposits on the north-central shore of the lake, and coarser
372 fluvial deposits in the east at the sampling site. While T1 and T3 profiles can be assumed to
373 represent a continuous sedimentation sequence, T2 profile displays an irregular interface at 1 m
374 depth that suggests an interruption in the sedimentation process potentially associated with
375 emersion and erosion (red line on Fig. 10b). For each profile, we collected two samples on the
376 surface of the terrace, and when possible, three to four samples in the first 1.5 m below the
377 surface, and one to two deeper samples at the bottom of the profile to constrain the potential
378 inherited nuclide content. We sampled pebbles made of silicate material in order to have ~100 g
379 of quartz per sample.

380 The beryllium was extracted at the Geo-thermo-chronology platform (ISTerre, University
381 Grenoble Alpes, France). Quartz was obtained from the 250-500 µm fraction after isolation of
382 the non-magnetic grains by repeated leaching in a H_2SiF_6-HCl mixture. The samples were then

processed following the chemical procedure of Brown et al. (1991) and Merchel and Herpers (1999). The beryllium was finally measured as a $^{10}Be/^{9}Be$ ratio at the ASTER Accelerator Mass Spectrometer in Aix-en-Provence, France (Arnold et al., 2010).

6.2 Age determination

The obtained concentration-depth-profiles (Table 5 and Fig. 11, 12, 13) were modelled with a Monte Carlo approach using the code ^{10}Be profile simulator version 1.2 developed by Hidy et al. (2010). This approach enables to find the combination of parameters that best fits the measured profile, including the exposure age, the erosion rate and the inherited TCN concentration. The validity of the method requires the following conditions: the TCN concentrations have not reached equilibrium with the landscape, the sampled profile corresponds to a unique episode of deposition and exposure with no vertical mixing, the inherited concentration is constant over the sampled depth range.

The halflife of ^{10}Be (1.387±0.012 Ma) was taken from Chmeleff et al. (2010). We used a global mean SLHL (sea level and high latitude) reference production rate of 4.06±0.23 atoms.g^{-1}.a^{-1} for the neutron induced spallogenic production using the CREp program (Martin et al., 2017), with the Lifton-Sato-Dunai scaling scheme (Lifton et al., 2014), the ERA40 atmosphere model (Uppala et al., 2005), and the Lifton VDM 2016 geomagnetic correction (Lifton, 2016). The muonic production was calculated using the theoretical equations of Heisinger et al. (2002a,b) and determined at the sampling site's elevation and for a given depth following the approach of Balco et al. (2008). The depth of muonic production fit was set at 5 cm. The error in 10Be half-life was set at 5%. The sampling sites were not associated with significant topographic/geometric shielding or additional cover. The cumulative bulk density of the material above each sample

405 was assumed constant over depth, with an average value of 2.2 g/cm^3, previously measured in
406 similar gravel-based terraces (Hidy et al., 2010). For the first iterations, the initial parameters for
407 age, inheritance and erosion rate were allowed to vary largely (age between 5-40 ka, erosion rate
408 below 3 cm/ka, and inheritance below 25.105 at/g). The total erosion threshold was set between
409 0 and 30 cm.

410

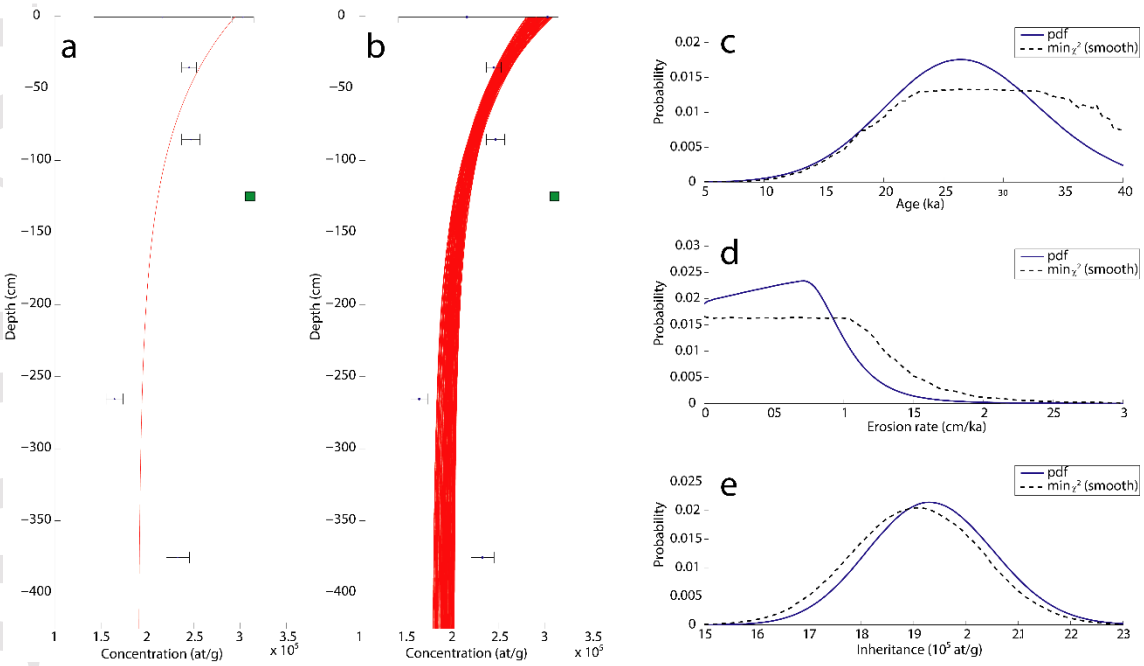

411

412 **Figure 11.** Result of the Monte Carlo simulations for terrace T1. (a) ^{10}Be concentrations
413 measured along depth and best fit obtained. (b) All the solutions found in the parameter solution
414 space defined as inputs. The sample excluded from the inversion is shown as a green box. (c, d,
415 e) Probability density functions (solid lines) and minimum χ^2 distributions (dashed line) for the
416 exposure age, erosion rate and inheritance concentration respectively.

417

Terrace T1 profile presents one point (15TUR4-130) with a high concentration, larger than the surface samples, which is incompatible with the theoretical depth profile. After excluding this sample, the algorithm was not able to find solutions in the 2σ confidence windows, and we had to increase the χ^2 cut-off value to 11. Although doing so prevented us from properly quantifying the error on the parameters, the best fits among the 250,000 solutions obtained provided a modal age of $\mathbf{27.0^{+10.9}_{-13.0}}$ ^{10}Be ka BP (Fig. 11), a low erosion rate ranging below 1 cm/ka, and a much higher inheritance around ~190,000 at/g.

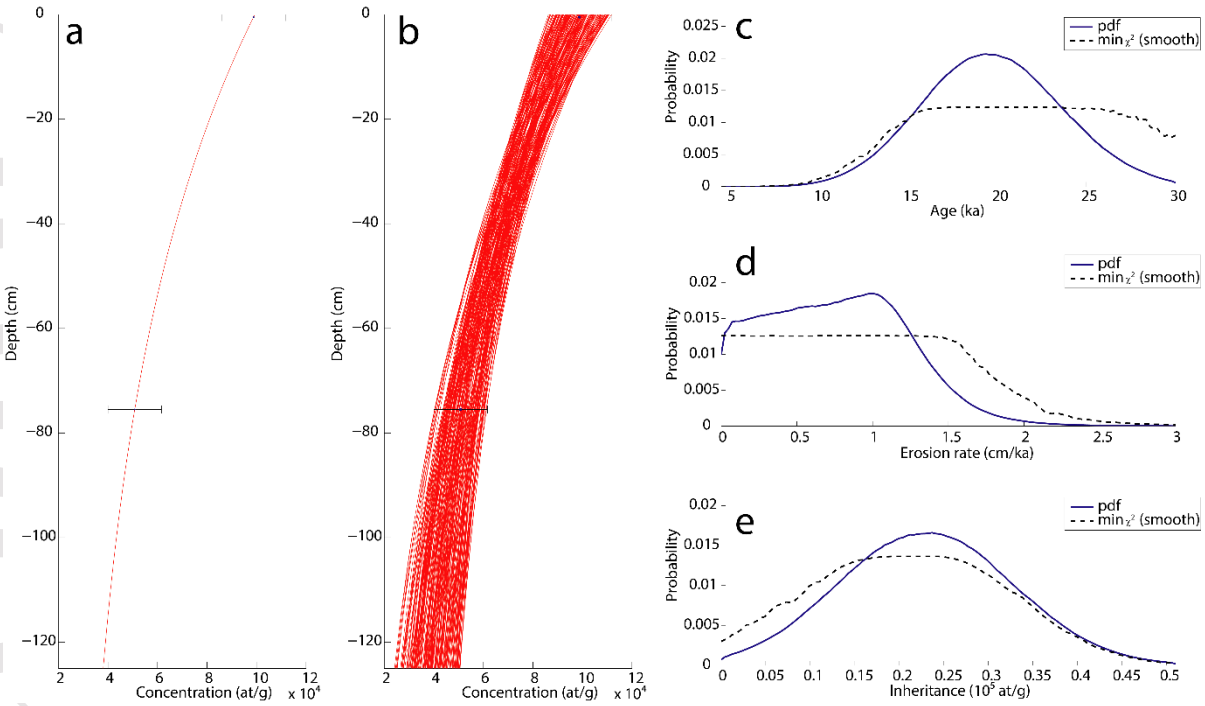

Figure 12. Result of the Monte Carlo simulations for terrace T2. (a) ^{10}Be concentrations measured along depth and best fit obtained. (b) All the solutions found in the parameter solution space defined as inputs. The three samples excluded from the inversion show concentrations above 120,000 at/g. (c, d, e) Probability density functions (solid lines) and minimum χ^2

distributions (dashed line) for the exposure age, erosion rate and inheritance concentration respectively.

Terrace T2 profile presents more complexity, especially because the two deepest samples (15TUR3-110 and 15TUR3-150) have the highest nuclide concentrations of all the dataset. As the outcrop stratigraphy suggests, they are likely to belong to a previous deposition sequence which was eroded before the onset of a new sedimentation sequence over it. The algorithm could only converge towards a solution after excluding these deep samples, and one surface sample (15TUR3-0a) showing a low nuclide concentration. With only two samples, it is impossible to determine statistically robust solutions for the age, erosion rate and inheritance at the same time. To narrow down the solution space, we constrained the initial inheritance using the concentration of sample 15TUR3-60 as upper bound, and the initial age below the age obtained for T1. We finally obtained 250,000 solutions within the 2σ confidence window, giving a most probable age of $\mathbf{19.6^{+7.7}_{-7.2}}$ ^{10}Be ka BP (Fig. 12).

For terrace T3, the simulator was not able to produce solutions when all the data of the profile were included, especially because one surface sample (15TUR5-0a) showed a very low concentration comparable to the deepest sample (15TUR5-130). We assumed this sample to be an outlier, likely to originate from recent excavation and deposition during agricultural work. We observed that the profile data did not permit to constrain the erosion rate. We tested initial maximum erosion rates of 1, 2 and 3 cm/kyr and obtained similar results between the three simulations. Using a moderate erosion rate of 1 cm/kyr as initial upper bound, the 250,000 solutions found within the 2σ confidence window gave a most probable age of $\mathbf{3.8^{+6.3}_{-2.7}}$ ^{10}Be ka BP. This involves an inheritance of ~8000 at/g (i.e. 30% of the surface sample) (Fig. 13e). Finally, we considered the possibility that additional exposure may happen under a shallow lake

water cover, which would lead to an overestimation of the age of subaerial exposure, as TCN started to accumulate before the total emersion and abandonment of the lake plain. A water depth of 4 m allows ~10% of the influx of cosmic rays to hit the sediments. To estimate the amplitude of this effect on the final age, we ran the simulation with the nuclide concentrations decreased by 10%. This correction resulted in a 16% younger age, which suggests that this effect remains small relative to the 2σ uncertainty range.

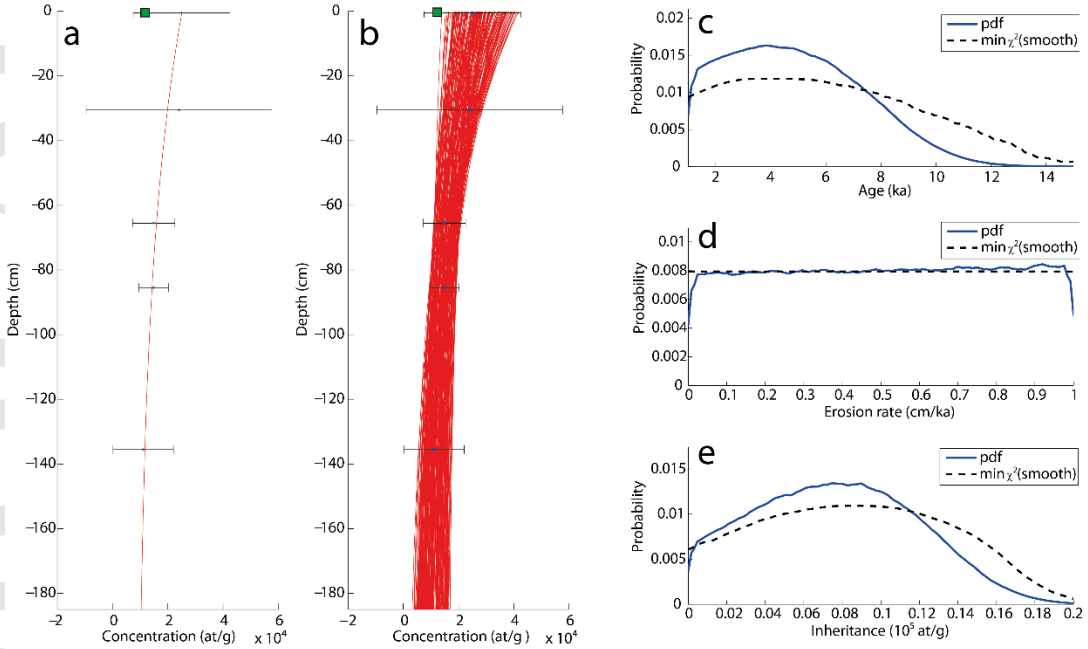

Figure 13. Result of the Monte Carlo simulations for terrace T3. (a) ^{10}Be concentrations measured along depth and best fit obtained. (b) All the solutions found in the parameter solution space defined as inputs. The sample excluded from the inversion is shown as a green box. (c, d, e) Probability density functions (solid lines) and minimum χ^2 distributions (dashed line) for the exposure age, erosion rate and inheritance concentration respectively.

7 Discussion

7.1 Horizontal slip rate estimate

Horizontal slip rates are usually constrained by dating sedimentary units laterally displaced by the faults (Hubert-Ferrari et al., 2002; Kozaci et al., 2007, 2009; Le Béon et al., 2010; Rizza et al., 2011; van der Woerd et al., 2006; Zabci et al., 2015). This kind of estimation is preferentially done with cumulative offsets of several hundreds of meters in order to average out the variability of individual coseismic displacements (see e.g. Wechsler et al., 2018). This type of measurement will yield a minimum slip rate as the offset is considered to be as old as the emplacement of the sediments, although it could also be much younger without a way for us to know about it.

Southeast of the lake, the MNAF segments have displaced Holocene streams incising in the low-gradient alluvial fans overlying terrace T3. Among the markers identified, the largest quality 1 offset measured is $\mathbf{16.5^{+2.5}_{-1.5}}$ m on a river located ~3.5 km west of Dirazali village (Fig. 9). The COPD results suggest that this corresponds to the cumulative slip of the last 3 to 4 large earthquakes. Deriving a slip-rate from this offset and our age of $\mathbf{3.8^{+6.3}_{-2.7}}$ ^{10}Be ka BP for T3 is hampered by two limitations. (i) The displaced stream may be significantly younger than the underlying lake plain, so the ratio between the mean offset and the age of T3 can only provide a minimum horizontal slip rate. (ii) The possible alluvial contribution at the sampling pit from the Dirazali fan must be assumed synchronous or older than the fan incised in by the offset stream. To propagate the 2σ asymmetric uncertainties in the slip rate calculation, we used the NIST Uncertainty Machine (https://uncertainty.nist.gov/; Lafarge and Possolo, 2016) with a Monte Carlo approach. We obtained a horizontal slip rate of $\mathbf{4.4^{+10.6}_{-2.8}}$ mm/yr. Although this value is in the same range as the rate of 3.7±0.7 mm/yr estimated by Gasperini et al. (2011) on Gemlik

segment, it is poorly constrained due to the young age and large relative uncertainty of T3.

7.2 Past seismic events evidenced along-strike

Our study of cumulative offsets along the MNAF provides valuable information on earthquake propagation along this fault, in terms of rupture extent, slip amount and distribution. It also allows us to discuss the behavior of the MNAF segments during the last major earthquakes.

If we assume the first two peaks to be the signature of the last two large earthquakes, with respective maximum coseismic slips of 6.2±2 m and 5.7±4 m, empirical scaling laws suggest that they correspond to events of moment magnitude of 7.2±0.2 to 7.4±0.2, with rupture lengths of 73±28 to 97±42 km (Wells & Coppersmith, 1994; using all-slip-type and strike-slip regressions respectively). Conversely, a rupture extending along the entirety of the 148 km long studies section would correspond to an earthquake of moment magnitude 7.6±0.3 and maximum coseismic displacements of 6.7-6.8 m, using the same scaling relationships. Our results are therefore compatible with large earthquakes able to rupture large parts of the eastern MNAF. Wesnousky (2006) has suggested that there exists a maximal step-over size (3-4 km fault-perpendicular) which tends to stop rupture propagation. However, this threshold has been crossed in recent examples (e.g. Fletcher et al., 2014; Hamling et al., 2017). In our case, Sölöz bend and Mekece, which are the largest identified step-overs of the eastern MNAF, have widths of 2.5 and 1.5 km respectively, and it can thus be assumed that past large ruptures may have propagated through them.

Our results show significant along-strike variability of the total number of recorded slip events

and the associated slip values. Mean slip values tend to be lower for segments C, D and E. We also note that segments D and E document more individual slip events than the other segments. It has been observed that the COPD curve shows an exponential decay in the peaks' amplitude with increasing cumulative slip (Klinger et al., 2011), as older markers tend to be less preserved in the landscape. We find this kind of pattern for some segments (e.g. segment C), but for segments B and G we observe that peak 1 is smaller than peak 2. The central segments are characterized by higher slopes. This implies more dynamic hydrologic conditions and geomorphic marker formation, and thus a higher capacity to preserve the traces of successive earthquakes (Zielke et al., 2015). By contrast, the lower slopes of the other segments may have favored more intensive agricultural activities, thus partly erasing traces of past ruptures. Therefore, a first possibility to explain the along-strike slip-per-event variability is to assume that COPD peak 1 on segments B, F and G is cumulative, and that the last event was not preserved enough on segments B, F and G to produce a strong COPD peak (Fig. 14b).

Alternatively, the slip decrease observed in the central segments may be related to their higher geometrical complexity (fault bends and obliquity, overlapping segments and branching, see sections 2 and 4.2). Distribution of the deformation across several structures implies that only part of the slip can be measured on the investigated MNAF strand, leading to apparent local slip decrease. A more oblique slip vector with a larger, unaccounted for vertical component, especially along segments C and D, may have a similar effect. Lower horizontal coseismic slip values along these segments may also suggest partial partitioning, with the subaqueous Iznik fault accommodating a part of the horizontal displacement (see e.g. de Michele et al., 2010; King et al., 2005 for recent examples of this). Finally, structural complexities may act as a barrier for the propagation of ruptures, leading to smaller offsets through slip tapering (King and Nabelek,

533 1985; Ward, 1997; Zielke et al., 2015).

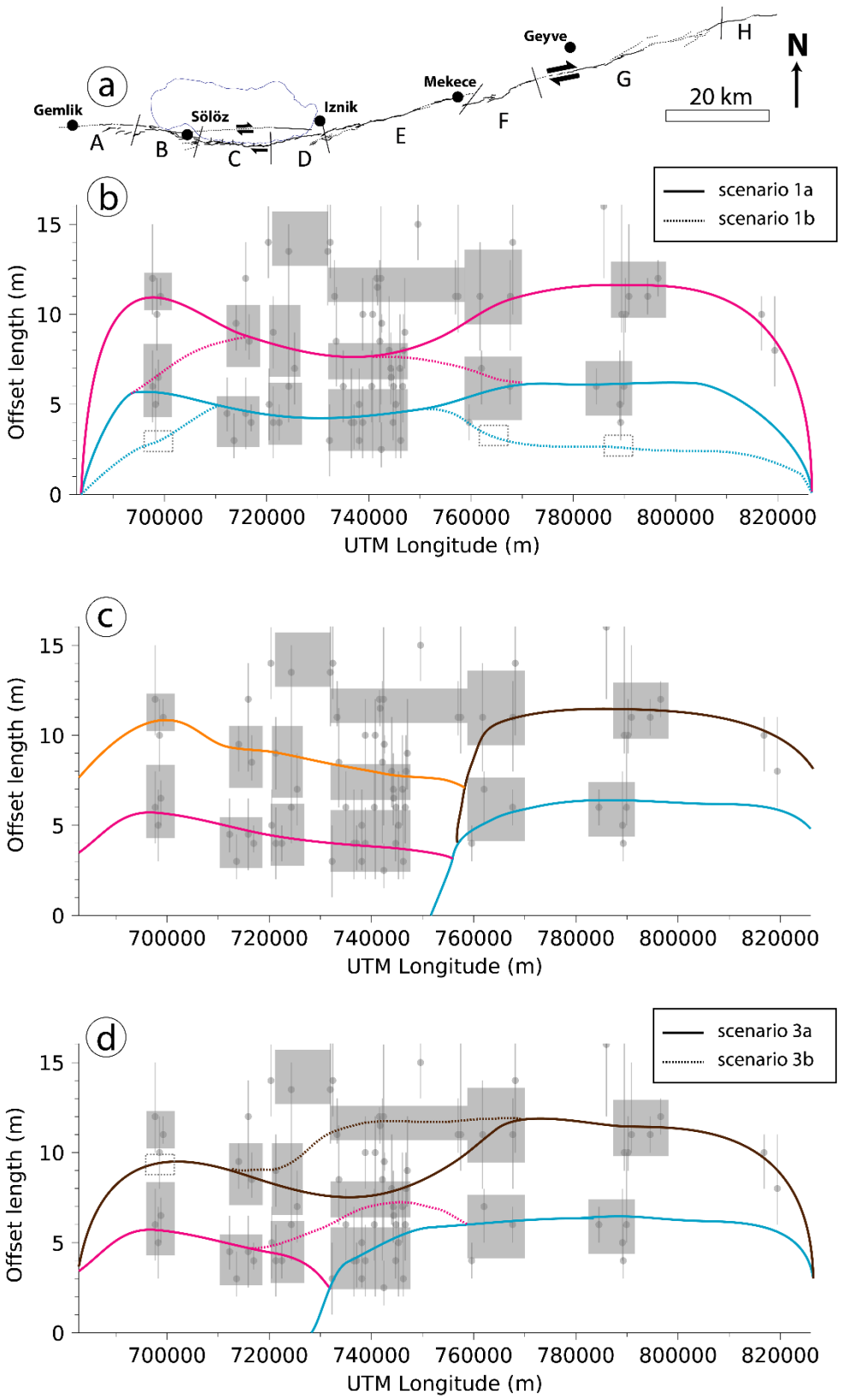

535 **Figure 14.** (a) Geometry of the fault section studied. (b) First order scenarios of horizontal slip
536 distribution during past events. The last major event (light blue) is assumed to have ruptured all
537 the segments. The penultimate (magenta) replicates this slip distribution. Alternative scenario 1b
538 assumes a partly unpreserved, smaller slip (broken boxes) for the last major rupture. (c) Scenario
539 2 of horizontal slip distribution. The last rupture is assumed to have propagated in the east of the
540 section studied and along segments F to H. The penultimate event propagated along the
541 remaining segments and further west. The previous events (brown and orange) replicate these
542 slip distributions. (d) Scenario 3 of horizontal slip distribution. The last ruptures propagated
543 partially along the MNAF and neighboring systems. The antepenultimate event (brown) was a
544 full MNAF rupture with a partly unpreserved smaller slip on segment A. Alternative scenario 3b
545 assumes overlapping traces for the last ruptures on segment D.
546

547 The combination of the coseismic slip variation along strike, the epistemic uncertainty affecting
548 offset measurements and the evolution of markers' morphology since the last event can limit the
549 interpretation of COPD peaks as representing individual earthquakes (Lin et al., 2020; Reitman
550 et al., 2019). Given that the last large earthquake along the MNAF happened before the 20th
551 century and was not accurately documented at the time, we ignore the typical range of variation
552 for the coseismic slip. The surface slip during 1999 Düzce and Izmit earthquakes on the NNAF
553 show coefficients of variation (CoV) of 0.5-0.6 (Akyüz et al., 2002; Barka et al., 2002). Such
554 values of CoV hardly enable to confidently recover more than one or two events or sequence of
555 events from the COPD curve and estimate the associated slip values. Therefore, higher COPD
556 peak values and increments, which come with higher uncertainty, should be considered with
557 caution. A couple of slip increments on segments B and E exceed 6.5 m (Table 4) and seem less

558 realistic given the magnitudes typically observed for recent earthquakes and estimated for
559 historical earthquakes in the Marmara region. Thus, we interpret those as being cumulative
560 contributions of two or more smaller, distinct events.

561 The slip history per segment resulting from our offset analysis does not unambiguously unravel
562 the past earthquakes succession along the MNAF. Alternative scenarios, with different numbers
563 of earthquakes, locations, lengths of ruptures, can be proposed that account equally for these
564 observations. Given the resolution of our satellite images and the uncertainties in our offset
565 measurements, our analysis can hardly detect individual offsets below 2.5 m and thus slip events
566 of Mw < 7. We cannot rule out that some smaller slip events were not resolved by our analysis,
567 which would add some local variability of the slip distribution in the possible scenarios. The
568 amount of slip involved in these events would logically be smaller as well, and so the
569 uncertainties associated with them would not fundamentally change the proposed scenarios.

570 To assess the possible scenarios, we require independent constraints about the location, age and
571 characteristics of past earthquakes along the MNAF. Fortunately, the seismicity of the MNAF
572 region of the last two millennia is documented by significant written accounts (see e.g.
573 Ambraseys, 2009), archeological evidence (Benjelloun et al., 2018, 2020) and a few
574 paleoseismological investigations (see section 3). According to the slip rate estimates (sections 3
575 and 7.1), this time frame should correspond to a cumulative horizontal slip ranging between 6
576 and 10 meters. This includes between one and three COPD peaks, depending on segments.

577

578

7.3 Independent constraints on historical earthquakes along the MNAF

7.3.1 Historical seismicity

At least five destructive ruptures are documented in the historical seismicity catalogues for the eastern part of the MNAF (Ambraseys, 2002, 2009; Ambraseys and Finkel, 1991, 1995; Ambraseys and Jackson, 1998; Guidoboni et al., 1994; Fig. 2; Table S1). These events come with high uncertainties on their location and magnitude, and it is generally difficult to locate the ruptured fault from historical data only. Most of the information available relates to the cities of Iznik and Gemlik. Excluding the earthquakes documented on the NNAF, Iznik was destroyed by local earthquakes around 29-32 CE (M_s 7), in 121 CE (M_s 7.4), in 368 CE (M_s 6.8), and 1065 CE (M_s 6.8). The region of Gemlik was affected by the M_s~7.2 1419 CE earthquake, which may have originated from the SNAF system as no effect was reported in Iznik. A series of minor ruptures, with estimated magnitudes about 5, are known between 1855 and 1863, also felt in Gemlik and along the southern shore of Iznik Lake.

7.3.2 Archeoseismology

Through an archeoseismological study in Iznik, Benjelloun et al. (2020) evidenced three episodes of seismic damage in the city since the Roman period: (1) between the early 6th and late 8th century CE, (2) between the mid-9th and late 11th century CE, and (3) after the late 14th century CE. These episodes were associated with a minimal intensity of VIII (EMS-98) in Iznik, suggesting earthquakes of at least Mw 6. The modeling of a standing Roman obelisk north of the city ruled out the occurrence of Mw > 7.2 ruptures along the fault section south of Iznik since the 1st century AD.

7.3.3 Paleoseismology

Paleoseismological trenching works have documented mid-19th century events on segments A and C. On segment A, a penultimate event was identified between the 12th and 18th centuries CE, but was not seen in trenches located south of Iznik Lake. A possibly contemporaneous event was also documented between the 14th and 18th centuries in a trench west of Mekece. On segment C, one penultimate event was documented after the late 7th century CE, and two older events were identified before the mid-5th century CE in two trenches (see section 3, Fig. 2c). South of Iznik Lake, Erginal et al. (2021) reported a 50 cm high coseismic scarplet in beachrock deposits that they attributed to an 8th century rupture.

Other important constraints can be derived from the lake core recently studied by Gastineau et al. (2021). These sedimentary archives recorded the occurrence of several major earthquakes documented both on the NNAF and MNAF, among which the 29-32 CE, 121 CE, 1065 CE, and an 8th century CE event. The 1065 CE earthquake ruptured a sublacustrine fault trace identified within Iznik Lake, north of the onshore segment D. No event was recorded in these cores in the eight centuries following the 1065 CE earthquake, which strongly supports the absence of Mw > 6.5 events on the central segments of the MNAF after 1065 CE. However, the lack of earthquake recording after 1065 may be due to too low sedimentation rates in the lake in the last millennium, even for large events located farther than 20-30 km from the lake.

7.3.4 Synthesis

The events documented by at least two types of record, include the 29-32 (M_s 7), 121 (M_s 7.4), 1065 (M_s 6.8) and 1419 (M_s 7.2) CE historical earthquakes. The precise location of the 1419 CE earthquake is not well constrained, but the fact that it was not recorded in the Iznik Lake cores

nor in trenches south of Iznik Lake, and that destructions were only reported in the region of Bursa, suggest that it did not extend east of Sölöz. To these we can add an 8th century event which affected the central MNAF segments south of Iznik Lake, and a 14th-18th century event attested by some damaged buildings in Iznik and one trench on segment E.

7.4 Analysis of COPD peak 1

In a first assumption (Fig. 14b, scenario 1a), COPD peak 1 can be interpreted as a large Mw 7.2-7.4 event rupturing the whole length of the studied fault. This first interpretation involves significant slip variations along strike, with slip values on the central segments C, D and E ~33% lower than on the other segments. The hypothesis of differential preservation across segments suggests another scenario (Fig. 14b, scenario 1b), with a more homogeneous slip of ~4 m along the studied section, only recovered on the central segments. Instead of decreasing slip on the central segments as in the scenario 1a, this scenario involves a maximum slip in the central area, which decrease towards both rupture tips. Given the higher structural complexity of this area, lower horizontal slip values are expected along the central segments. Therefore, scenario 1a can be considered more likely than scenario 1b. The favored historical candidate is the 1065 CE earthquake, which is the best documented event. However, this means that the magnitude of the 1065 CE earthquake, estimated at 6.8 by historical seismology studies, should be significantly raised, by at least 0.3 units. It also implies that the 1065 CE rupture identified in Iznik lake propagated along the onshore fault segments as well. In addition, the deformation of the obelisk north of Iznik does not support magnitudes over Mw 7.2 for events located south of Iznik, but might be accounted for with a more distant epicenter, located on the western or eastern segments

644 (Benjelloun et al., 2020).

645 Another possibility is to propose earthquakes rupturing only a part of the studied MNAF section,
646 with the central segments acting as a slip barrier (Fig. 14c, d). Following this hypothesis, COPD
647 peak 1 would correspond to two different earthquakes. These earthquakes ruptured different
648 sections of the fault, either adjacent (scenarios 2 and 3a) or overlapping (scenario 3b). The lower
649 slip values on the central segments are associated with the termination of earthquakes. In this
650 case, no significant slip variation appears along strike. The high slip values imply that the
651 ruptured area during these earthquakes could be respectively extended west of Gemlik and east
652 of the junction with the main NAF strand. This interpretation best accounts for the multiple
653 events found in the different records of past seismicity. The 1065 CE earthquake is a favored
654 candidate for the western and central segments. The historical seismicity of the east of the
655 studied area is less documented, but the 14^{th}-18^{th} c. event found in the archeological and
656 paleoseismic record is a possible candidate for the eastern rupture of this scenario.

657

658 **7.5 Analysis of COPD peak 2 and implications for the long-term behavior of the MNAF**

659 The increments between COPD peaks 1 and 2 suggest that the slip values of the last and
660 penultimate events (or sequences of events) were comparable. Although the slip values estimated
661 for the penultimate event come with higher uncertainties, they also suggest magnitudes as high
662 as Mw 7.4±0.2. The lacustrine record documents at least two events in the first centuries CE
663 (Gastineau et al., 2021). The historical catalogues include two candidates, in 29-32 CE and in
664 121 CE, with poorly constrained locations along the MNAF. Both events can be accounted for
665 by interpreting peak 2 as two distinct ruptures (scenario 2, Fig. 14c). Given the uncertainties, a

full MNAF rupture may also be proposed (scenarios 1 and 3, Fig. 14b and d).

The reconstructions of along-fault slip accumulation derived from systematic offset measurements have been associated to the development of earthquake recurrence models (Schwartz & Coppersmith, 1984; Zielke et al., 2015). In our case, given the large uncertainties, the successive increments on each segment cannot be unambiguously discriminated. Our dataset remains compatible with a "characteristic slip" behavior, as in scenarios 1 and 2 (Fig. 14b, c), where the earthquakes show recurring, similar slip distributions (see e. g. Klinger et al., 2011; Kurtz et al., 2018; Zielke et al., 2010). In scenarios 1a and 2, the horizontal cumulative slip on segments C, D and E is 25-35% lower than on the other segments for the last two events. This cumulative slip deficit on the central segments produces a higher apparent slip rate variation along-strike. The interpretations of scenario 3 depart from the characteristic slip model, as the proposed distributions of the last events differ from the previous one, which resembles a variable slip model.

The Late Quaternary slip accumulation along the MNAF seems dominated by large events with comparable per-segment slip increments. This corresponds to the synoptic model of Zielke et al. (2015), which also considers the occurrence of smaller ruptures contributing marginally to the overall slip accumulation. The 8th century CE event reported south of Iznik Lake (Erginal et al., 2021), and the 19th century CE earthquakes reported in Gemlik (Özalp et al., 2013) may illustrate these features. Future trenching work is needed to document the timing of earthquakes and to judge between both models.

688 **7.6 Possible interactions between the NAF strands for the historical period**

689 In all the scenarios discussed, we can propose that the eastern MNAF has experienced two major
690 sequences of ruptures in the last two millennia. These historical sequences correspond to large
691 magnitude events, with amounts of slip ranging between 3.2 and 6.2 m. Most of the deformation
692 was produced during intervals of high seismic activity, separated by longer quiescent periods
693 (1000-1500 years). This can be compared to the rupture history of other strike-slip fault systems
694 such as the San Andreas and Dead Sea faults (Lefevre et al., 2018; Rockwell et al., 2014). This
695 long recurrence time contrasts with the historical behavior of the NNAF (Fig. 2), and is
696 consistent with a slip rate ~5 times smaller on the MNAF. In the final part of this discussion, we
697 replace our propositions of past rupture history in the wider frame of the eastern Marmara region.

698 The last sequence of high seismicity along the MNAF, whatever the scenario considered, seems
699 to occur between the 11th and 18th centuries, while the northern strand of the NAF along the
700 Izmit Gulf (between 29.2° and 30.3°E) knew a period of lower seismic activity (Fig. 2b). The
701 1065 CE earthquake was preceded by a major event on the NNAF in 1063 CE. However, it
702 mainly affected the western part of the Marmara region, with no significant damage reported east
703 of Constantinople (Ambraseys, 2009). Between the 14th and 18th centuries, only one major
704 earthquake is known for the eastern Marmara region in 1509 CE (M~7.2). The Gulf of Izmit was
705 likely affected by this earthquake (Klinger et al., 2003), but the contemporary historical records
706 do not account for heavy damage farther east (Ambraseys, 2001b). After this earthquake, a
707 quiescence period is reported for the Marmara region between 1509 and 1719 CE (Ambraseys &
708 Jacskon, 2000; Pondard et al., 2007; Rockwell et al., 2009).

709 By contrast, the southern strands of the NAF were marked by a significant seismic activity in the

east of the Marmara Sea. After the 1065 CE earthquake on the MNAF, this activity seems to restart in the early 15th century CE. It includes the 1419 CE earthquake which affected the Bursa region, and the event proposed between the 14th and 18th centuries CE along the eastern segments of the MNAF (scenarios 2 and 3). This earthquake may have propagated across the junction with the main NAF strand. The junction zone does not present any significant step-over, but only an azimuth change of ~20°. The 1967 CE earthquake propagated across this junction between the main NAF and the NNAF, with a similar azimuth difference. Therefore, a symmetrical rupture between the main NAF and the MNAF is not unrealistic. A trenching study carried out by Palyvos et al. (2007) in the Mudurnu valley, located a few kilometers east of the junction with the main NAF strand, identified at least one and most probably two paleoevents younger than 1693 CE. Some of these ruptures may have propagated across the junction along the MNAF. Analogous alternations of active and quiescent phases between adjacent fault strands have been previously identified on the San Andreas fault system in relation to the San Jacinto fault (Lozos, 2016; Onderdonk et al., 2018). In the case of the NAF in the Marmara region, the investigation of older sedimentary records of past earthquakes on the different strands might better document this behavior and check for earlier occurrences of it.

8 Conclusion

By combining field observations and the analysis of high-resolution satellite images, we have demonstrated that the segments constituting the MNAF in the southeast of the Marmara region have been significantly active during the Holocene. The fault displays morphological features typical of strike-slip deformation, associated locally with a smaller vertical component. We

collected 114 measurements of horizontally offset markers, providing evidence for large, repeated earthquakes along the MNAF. Through a statistical analysis of the offsets, we particularly documented at least two major surface-rupturing earthquakes whose deformation was preserved in the landscape. They are characterized by coseismic horizontal displacement ranging from 3.2 to 6.2 m, which indicates moment magnitudes ranging between 7.2±0.2 and 7.4±0.2 according to empirical scaling laws. Some of these events may have ruptured the whole eastern MNAF section along more than 100 km. Although smaller earthquakes also happened in the past, our analysis may not resolve accurately their frequency due to the data uncertainties and preservation issues. According to the historical catalogues of seismicity and paleoseismological studies, the last large events documented along this fault strand possibly happened in 1065 CE, or between the 14th and 18th centuries CE along the eastern segments. These intervals correspond to a period of relative quiescence along the NNAF segments located east of the Marmara Sea. We estimated a late Holocene horizontal slip rate of $\mathbf{4.4^{+10.6}_{-2.8}}$ mm/yr on the central MNAF segments. Since the last large events, the eastern MNAF segments may have accumulated stress equivalent to 1-4 m of horizontal deformation. Therefore, the current level of stress may be enough to generate a significant earthquake, comparable or larger than a 1065 CE type rupture, which caused important damage in Iznik. The activity of the southern strands of the NAF should not be neglected in terms of slip history and should be considered into any seismic hazard assessment.

Data Availability Statement

The bathymetric map of Marmara was made available by the EMODnet Bathymetry project

(https://www.emodnet.eu/bathymetry), using the EMODnet Bathymetry portal (EMODnet Bathymetry Consortium, 2016, EMODnet Digital Bathymetry [DTM], DOI: 10.12770/c7b53704-999d-4721-b1a3-04ec60c87238) funded by the European Commission Directorate General for Maritime Affairs and Fisheries. The large-scale topography of the study area was obtained from the Shuttle Radar Topography Mission 1 Arc-Second Global (DOI:10.5066/F7PR7TFT). The bathymetry of İznik Lake was provided by and can be obtained from the Turkish General Directorate of Hydraulic Works (DSI). Pleiades imagery is available for purchase from Airbus industry (https://www.intelligence-airbusds.com/en/8692- pleiades). The full offset retro-deformation dataset and a vector file of the fault map are available on the Zenodo repository (Benjelloun et al., 2021) [open access]. The maps of Figures 5 are from Google Earth satellite imagery. The diagrams of Figures 6, 7, 8 and 14 were prepared using the Matplotlib 3.3.0 package for Python (https://matplotlib.org/; Hunter, 2007). All websites were last accessed in January 2021. Supporting Information for this article includes a detailed explanation of the marker quality score determination, a list of historical earthquakes in the area of interest, a summary of paleoseismic trenching works done in the area, the offset measurement data, and supplementary figures on the vertical slip markers south of Iznik Lake, some field examples of Quaternary faulting, and the automatic fault discretization procedure.

Acknowledgments

This work has been supported by the Mediterranean Integrated STudies at Regional And Local Scales – ENVIronment of the MEDiterranean (MISTRALS-ENVIMED) program (The North Anatolian Fault in the region Iznik: Geomorphological Evolution and Archaeoseismicity

[NAFIGEA] project), the Institut National des Sciences de l'Univers (INSU) Aleas program (France), and the ANR CE03-2019 Basiliznik-secrets. The Pleiades images were bought with support from LabEx OSUG@2020 (Investissements d'avenir – ANR10 LABX56, France). This study contributes to the IdEx Université de Paris ANR-18-IDEX-0001. The authors warmly thank the ASTER team (D. Bourlès, G. Aumaitre, K. Keddadouche, and R. Braucher) for the measurements performed at the ASTER AMS facility (CEREGE, Aix-en-Provence). We thank the Turkish Ministry of Culture and Tourism for allowing the field work. We thank Pr. Mustafa Sahin and his research group, and the Kandilli observatory in Iznik for their help with logistics and housing. The authors declare no conflict of interests.

References

Aki, K. (1984). Asperities, barriers, characteristic earthquakes and strong motion prediction. *Journal of Geophysical Research: Solid Earth*, 89(B7), 5867–5872.

Akyüz, S., Dogan, B., Aksoy, M. E., Tigli, O., & Zabci, C. (2014). *Preliminary Palaeoseismological results of the Middle Strand of the North Anatolian Fault (NAF) in the Marmara Region, NW Turkey.* Paper presented at European Geosciences Union General Assembly, Vienna, Austria.

Akyüz, H. S., Hartleb, R., Barka, A., Altunel, E., Sunal, G., Meyer, B., & Armijo, R. (2002). Surface rupture and slip distribution of the 12 November 1999 Düzce earthquake (M 7.1), North Anatolian fault, Bolu, Turkey. *Bulletin of the Seismological Society of America*, 92(1), 61-66. https://doi.org/10.1785/0120000840

Akyuz, H. S. & Zabci, C. (2012). *A review of paleoseismic investigations along the North*

Anatolian Fault, Turkey. Paper presented at PANAF: Paleoseismology Along the North Anatolian Fault Meeting, Istanbul, Turkey.

Ambraseys, N. N. (1970). Some Characteristic Features of the Anatolian Fault Zone. *Tectonophysics*, 9, 143-165. https://doi.org/10.1016/0040-1951(70)90014-4

Ambraseys, N. (2000). The Seismicity of the Marmara Sea Area 1800-1899. *Journal of Earthquake Engineering*, 4(3), 377–401. https://doi.org/10.1080/13632460009350376

Ambraseys, N. N. (2001a). Reassessment of earthquakes, 1900–1999, in the eastern Mediterranean and the Middle East. *Geophysical Journal International*, 145(2), 471–485. https://doi.org/10.1046/j.0956-540x.2001.01396.x

Ambraseys, N. N. (2001b). The Earthquake of 1509 in the Sea of Marmara, Turkey, Revisited. *Bulletin of the Seismological Society of America*, 91(6), 1397-1416. https://doi.org/10.1785/0120000305

Ambraseys, N. (2002). The seismic activity of the Marmara Sea region over the last 2000 years. *Bulletin of the Seismological Society of America*, 92(1), 1–18. https://doi.org/10.1785/0120000843

Ambraseys, N. (2009). *Earthquakes in the Mediterranean and Middle East. A multidisciplinary study of seismicity up to 1900.* Cambridge: Cambridge University Press. https://doi.org/10.1017/CBO9781139195430

Ambraseys, N. & Finkel, C. (1991). Long-term seismicity of Istanbul and of the Marmara Sea region. *Terra Nova*, 3(5), 527–539. https://doi.org/10.1111/j.1365-3121.1991.tb00188.x

Ambraseys, N. N., & Finkel, C. F. (1995). The Seismicity of Turkey and Adjacent Areas: A

Historical Review, 1500–1800. Istanbul: Muhittin Salih Eren.

Ambraseys, N. N., & Jackson, J. (1998). Faulting associated with historical and recent earthquakes in the eastern Mediterranean region. *Geophysical Journal International*, 133(2), 390–406. https://doi.org/10.1046/j.1365-246X.1998.00508.x

Ambraseys, N.N., & Jackson, J.A. (2000). Seismicity of the Sea of Marmara (Turkey) since 1500. *Geophysical Journal International*, 141(3), F1-F6. https://doi.org/10.1046/j.1365-246x.2000.00137.x

Ambraseys, N. N., Jackson, J. A., & Melville, C. P. (2002). Historical Seismicity and Tectonics: The Case of the Eastern Mediterranean and the Middle East. In W. H. K. Lee, H. Kanamori, P. C. Jennings, C. Kisslinger (Eds.). *International Handbook of Earthquake and Engineering Seismology* (Part A, pp. 747-763). Cambridge, MA: Academic Press. https://doi.org/10.1016/S0074-6142(02)80248-0

Ansberque, C., Bellier, O., Godard, V., Lasserre, C., Wang, M., Braucher, R., et al. (2016). The Longriqu fault zone, eastern Tibetan Plateau: Segmentation and Holocene behavior. *Tectonics*, 35(3), 565–585.

Antoine, S. L., Klinger, Y., Delorme, A., Wang, K., Bürgmann, R., & Gold, R. (2021). Diffuse Deformation and Surface Faulting Distribution from Submetric Image Correlation along the 2019 Ridgecrest, California, Ruptures. *Bulletin of the Seismological Society of America*, https://doi.org/10.1785/0120210036

Armijo, R., Meyer, B., Hubert, A., & Barka, A. A. (1999). Westward propagation of the North Anatolian fault into the northern Aegean: Timing and kinematics. *Geology*, 27, 267–270. https://doi.org/10.1130/0091-7613(2000)28<188:WPONAF>2.0.CO;2

Armijo, R., Meyer, B., King, G. C. P., Rigo, A., & Papanastassiou, D. (1996). Quaternary evolution of the Corinth Rift and its implications for the Late Cenozoic evolution of the Aegean. *Geophysical Journal International*, 126(1), 11-53. https://doi.org/10.1111/j.1365-246X.1996.tb05264.x

Armijo, R., Meyer, B., Navarro, S., King, G., & Barka, A. (2002). Asymmetric slip partitioning in the Sea of Marmara pull-apart: a clue to propagation processes of the North Anatolian Fault? *Terra Nova*, 14(2), 80–86. https://doi.org/10.1046/j.1365-3121.2002.00397.x

Arnold, M., Merchel, S., Bourlès, D. L., Braucher, R., Benedetti, L., Finkel, R. C., et al. (2010). The French accelerator mass spectrometry facility ASTER: Improved performance and developments. *Nuclear Instruments and Methods in Physics Research Section B: Beam Interactions with Materials and Atoms*, 268, 1954-1959. https://doi.org/10.1016/j.nimb.2010.02.107

Balco, G., Stone, J. O., Lifton, N. A., & Dunai, T. J. (2008). A complete and easily accessible means of calculating surface exposure ages or erosion rates from ^{10}Be and ^{26}Al measurements. *Quaternary Geochronology*, 3(3), 174 – 195. https://doi.org/10.1016/j.quageo.2007.12.001

Baris, S., Ito, A., Üçer, S. B., Honkura, Y., Kafadar, N., Pektas, R., et al. (2002). Microearthquake Activity before the Izmit Earthquake in the Eastern Marmara region, Turkey (1 January 1993-17 August 1999). *Bulletin of the Seismological Society of America*, 92(1), 394–405. https://doi.org/10.1785/0120000826

Barka, A. (1992). The North Anatolian fault zone. *Annales Tectonicae*, 6, 164–195.

Barka, A. (1993). *Kuzey Anadolu Fayı'nın Sapanca-Izmit ve Geyve-Iznik Kolları üzerinde Palaeosismik Arastırmalar* (Technical Report YBAG-4/7551). Istanbul: TÜBITAK.

Barka, A. (1996). Slip distribution along the North Anatolian fault associated with the large earthquakes of the period 1939 to 1967. *Bulletin of the Seismological Society of America*, 86(5), 1238–1254.

Barka, A., Akyüz, H. S., Altunel, E., Sunal, G., Cakir, Z., Dikbas, A., et al. (2002). The Surface Rupture and Slip Distribution of the 17 August 1999 Izmit Earthquake (*M* 7.4), North Anatolian Fault. *Bulletin of the Seismological Society of America*, 92(1), 43-60. https://doi.org/10.1785/0120000841

Barka, A. & Kadinsky-Cade, K. (1988). Strike-slip fault geometry in Turkey and its influence on earthquake activity. *Tectonics*, 7(3), 663–684.

Beauprêtre, S., Garambois, S., Manighetti, I., Malavieille, J., Sénéchal, G., Chatton, M., et al. (2012). Finding the buried record of paste earthquakes with GPR-based palaeoseismology: a case study on the Hope fault, New Zealand. *Geophysical Journal International*, 189(1), 73-100. https://doi.org/10.1111/j.1365-246X.2012.05366.x

Beauprêtre, S., Manighetti, I., Garambois, S., Malavieille, J., & Dominguez, S. (2013). Stratigraphic architecture and fault offsets of alluvial terraces at Te Marua, Wellington fault, New Zealand, revealed by pseudo-3D GPR investigation. *Journal of Geophysical Research: Solid Earth*, 118, 4564-4585.

Benjelloun, Y., de Sigoyer, Dessales, H., Baillet, L., Guéguen, P., & Sahin, M. (2020). Historical Earthquake Scenarios for the Middle Strand of the North Anatolian Fault Deduced from Archeo-Damage Inventory and Building Deformation Modeling. *Seismological Research Letters*, 92, 583-598. https://doi.org/10.1785/0220200278

Benjelloun, Y., de Sigoyer, J., Dessales, H., Garambois, S., & Sahin, M. (2018). Construction

history of the aqueduct of Nicaea (Iznik, NW Turkey) and its on-fault deformation viewed from archaeological and geophysical investigations. *Journal of Archaeological Science: Reports*, 21, 389-400. https://doi.org/10.1016/j.jasrep.2018.08.010

Benjelloun, Y., de Sigoyer, J., Garambois, S., Carcaillet, J., & Klinger, Y. (2021). Data for: Segmentation and Holocene Behavior of the Middle Strand of the North Anatolian Fault (NW Turkey) (Version 1.2.0) [Data set]. Zenodo. http://doi.org/10.5281/zenodo.5566874

Broxton, M. J. & Edwards, L. J. (2008). *The Ames Stereo Pipeline: Automated 3D Surface Reconstruction from Orbital Imagery*. Paper presented at the 39th Lunar and Planetary Science Conference, League City, TX.

Brown, E. T., Edmond, J. M., Raisbeck, G. M., Yiou, F., Kurz, M. D., & Brook, E. J. (1991). Examination of surface exposure ages of Antarctic moraines using in situ produced ^{10}Be and ^{26}Al. *Geochimica et Cosmochimica Acta*, 55, 2269-2283. https://doi.org/10.1016/0016-7037(91)90103-C

Chaput, E. (1936). *Voyages d'études géologique et géomorphogéniques en Turquie*. Paris : De Boccard.

Chmeleff, J., von Blanckenburg, F., Kossert, K., & Jakob, D. (2010). Determination of the ^{10}Be half-life by multicollector ICP-MS and liquid scintillation counting. *Nuclear Instruments and Methods in Physics Research Section B: Beam Interactions with Materials and Atoms*, 268(2), 192–199. https://doi.org/10.1016/j.nimb.2009.09.012

Choi, J. H., Klinger, Y., Ferry, M., Ritz, J. F., Kurtz, R., Rizza, M. et al. (2018). Geologic Inheritance and Earthquake Rupture Processes: The 1905 M ≥ 8 Tsetserleg-Bulnay Strike-Slip Earthquake Sequence, Mongolia. *Journal of Geophysical Research: Solid Earth*, 123.

https://doi.org/10.1002/2017JB013962.

Civico, R., Smedile, A., Pantosti, D., Cinti, F. R., De Martini, P. M., Pucci, S., et al. (2021). New trenching results along the Iznik segment of the central strand of the North Anatolian Fault (Turkey): an integration with preexisting data. *Mediterranean Geoscience Reviews*, 3, 115-128. https://doi.org/10.1007/s42990-021-00054-9

de Michele, M., Raucoules, D., de Sigoyer, J., Pubellier, M., & Chamot-Rooke, N. (2010). Three-dimensional surface displacement of the 2008 May 12 Sichuan earthquake (China) derived from Synthetic Aperture Radar: evidence for rupture on a blind thrust. *Geophysical Journal International*, 183(3), 1097-1103. https://doi.org/10.1111/j.1365-246X.2010.04807.x

Dikbas, A., Akyüz, H. S., Meghraoui, M., Ferry, M., Altunel, E., Zabci, C., et al. (2018). Paleoseismic history and slip rate along the Sapanca-Akyazi segment of the 1999 Izmit earthquake rupture (MW=7.4) of the North Anatolian Fault (Turkey). *Tectonophysics*, 738-739, 92-111. https://doi.org/10.1016/j.tecto.2018.04.019

Dogan, B. (2010). *Kuzey Anadolu Fay Sistemi Güney Kolunun Geyve-Gemlik Arasindaki Kesiminin Morfotektonik, Tektonostratigrafik ve Palaeosismolojik Evrimi*. (Doctoral dissertation). Istanbul: Istanbul Teknik Üniversitesi.

Elliott, J. R., Walters, R. J., & Wright, T. J. (2016). The role of space-based observation in understanding and responding to active tectonics and earthquakes. *Nature Communications*, 7, 13844. https://doi.org/10.1038/ncomms13844

Emre, Ö., Duman, T. Y., & Özalp, S. (2011*). 1:250.000 Ölçekli Türkiye Diri Fay Haritası Serisi*. (Technical report). Ankara: Maden Tetkik ve Arama Genel Müdürlügü.

Erginal, A. E., Erenoglu, R. C., Yildirim, C., Selim, H., H., Kiyak, N. G, Erenoglu, O, et al.

(2021). Co-seismic beachrock deformation of 8th century CE Earthquake in Middle Strand of North Anatolian Fault, Lake Iznik, NW Turkey. *Tectonophysics*, 799, 2286990. https://doi.org/10.1016/j.tecto.2020.228690

Ergintav, S., Reilinger, R. E., Çakmak, R., Floyd, M., Cakir, Z., Dogan, U., et al. (2014). Istanbul's earthquake hot spots: Geodetic constraints on strain accumulation along faults in the Marmara seismic gap. *Geophysical Research Letters*, 41(16), 5783–5788. https://doi.org/10.1002/2014GL060985

Flerit, F., Armijo, R., King, G. C. P., Meyer, B., & Barka, A. (2003). Slip partitioning in the Sea of Marmara pull-apart determined from GPS velocity vectors. *Geophysical Journal International*, 154(1), 1–7. https://doi.org/10.1046/j.1365-246X.2003.01899.x

Fletcher, J. M., Teran, O. J., Rockwell, T. K., Oskin, M. E., Hudnut, K., W., Mueller, K. J., et al. (2014). Assembly of a large earthquake from a complex fault system: Surface rupture kinematics of the 4 April 2010 El Mayor – Cucapah (Mexico) M_w 7.2 earthquake. *Geosphere*, 10(4), 797-827. https://doi.org/10.1130/GES00933.1

Fraser, J., Vanneste, K., & Hubert-Ferrari, A. (2010). Recent behavior of the North Anatolian Fault: Insights from an integrated palaeoseismological data set. *Journal of Geophysical Research: Solid Earth*, 115(B9): B09316.

Fu, B., Ninomiya, Y., Lei, X., Toda, S., & Awata, Y. (2004). Mapping active fault associated with the 2003 Mw 6.6 Bam (SE Iran) earthquake with ASTER 3D images. *Remote Sensing of Environment*, 92(2), 153–157. https://doi.org/10.1016/j.rse.2004.05.019

Gastineau, R., de Sigoyer, J., Sabatier, P., Fabbri, S. C., Anselmetti, F. S., Develle, A. L., et al. (2021). Active subaquatic fault segments in Lake Iznik along the middle strand of the North

Anatolian Fault, NW Turkey. *Tectonics*, 40, e2020TC006404.

Gasperini, L., Polonia, A., Çagatay, M. N., Bortoluzzi, G., & Ferrante, V. (2011). Geological slip rates along the North Anatolian Fault in the Marmara region. *Tectonics*, 30(6), TC6001.

Gold, P. O., Oskin, M. E., Elliott, A. J., Hinojosa-Corona, A., Taylor, M. H., Kreylos, O., & Cowgill, E. (2013). Coseismic slip variation assessed from terrestrial lidar scans of the El Mayor-Cucapah surface rupture. *Earth and Planetary Science Letters*, 366, 151-162. https://doi.org/10.1016/j.epsl.2013.01.040

Grall, C., Henry, P., Thomas, Y., Westbrook, G.K., Çağatay, M.N., Marsset, B., et al. (2013). Slip rate estimation along the western segment of the Main Marmara Fault over the last 405–490 ka by correlating mass transport deposits. *Tectonics*, 32, 2012TC003255. doi:10.1002/2012TC003255.

Guidoboni, E., and Comastri, A. (Eds.) (2005). *Catalogue of Earthquakes and Tsunamis in the Mediterranean Area From the 11th to the 15th Century*. Roma: Istituto Nazionale di Geofisica e Vulcanologia.

Guidoboni, E., Comastri, A., & Traina, G. (1994). Catalogue of ancient earthquakes in the Mediterranean area up to the 10th century. Roma: Istituto Nazionale di Geofisica.

Gürbüz, C., Aktar, M., Eyidogan, H., Cisternas, A., Haessler, H., Barka, A., et al. (2000). The seismotectonics of the Marmara region (Turkey): results from a microseismic experiment. *Tectonophysics*, 316(1), 1–17. https://doi.org/10.1016/S0040-1951(99)00253-X

Hamling, I. J., Hreinsdottir, S., Clark, K., Elliott, J., Liang, C., Fielding, E., et al. (2017). Complex multifault rupture during the 2016 7.8 Kaikoura earthquake, New Zealand. *Science*, 356(6334), eaam7194. DOI: 10.1126/science.aam7194

Heisinger, B., Lal, D., Jull, A., Kubik, P., Ivy-Ochs, S., Knie, K., & Nolte, E. (2002a), Production of selected cosmogenic radionuclides by muons: 2. capture of negative muons. *Earth and Planetary Science Letters*, 200(3), 357 – 369. https://doi.org/10.1016/S0012-821X(02)00641-6

Heisinger, B., Lal, D., Jull, A., Kubik, P., Ivy-Ochs, S., Neumaier, S., Knie, K., Lazarev, V., & Nolte, E. (2002b). Production of selected cosmogenic radionuclides by muons: 1. fast muons. *Earth and Planetary Science Letters*, 200(3), 345 – 355. https://doi.org/10.1016/S0012-821X(02)00640-4

Hidy, A. J., Gosse, J. C., Pederson, J. L., Mattern, J. P., & Finkel, R. C. (2010). A geologically constrained Monte Carlo approach to modeling exposure ages from profiles of cosmogenic nuclides: An example from Lees Ferry, Arizona. *Geochemistry, Geophysics, Geosystems*, 11(9), Q0AA10. https://doi.org/10.1029/2010GC003084

Honkura, Y. & Isikara, A. M. (1991). Multidisciplinary research on fault activity in the western part of the North Anatolian Fault Zone. *Tectonophysics*, 193(4), 347–357. https://doi.org/10.1016/0040-1951(91)90343-Q

Hubert-Ferrari, A., Barka, A., Jacques, E., Nalbant, S. S., Meyer, B., Armijo, R., et al. (2000). Seismic hazard in the Marmara Sea region following the 17 August 1999 Izmit earthquake. *Nature*, 404(6775), 269–273. https://doi.org/10.1038/35005054

Hubert-Ferrari, A., King., G., van der Woerd, J., Villa, I., Altunel, E., & Armijo, R. (2002). Long-term evolution of the North Anatolian Fault: new constraints from its eastern termination. In D. J. J. van Hinsbergen, M. A. Edwards, R. Govers (Eds.), *Collision and Collapse at the Africa-Arabia-Eurasia Subduction Zone*, *Geological Society Special Publications* (Vol. 311, pp.

133-154). London: The Geological Society. doi: 10.1144/SP311.5

Hunter, J. D. (2007). Matplotlib: A 2D graphics environment. *Computing in Science & Engineering*, 9, 90–95. https://doi.org/10.1109/MCSE.2007.55

Ikeda, Y. (1988). Recent activity of the Iznik-Mekece fault at Corak Stream, east of Iznik. In Y. Honkura,A. M. Isikara (Eds.), *Multidisciplinary research on fault activity in the western part of the North Anatolian Fault Zone* (pp. 15–27). Tokyo: Institute of Technology.

Ikeda, Y. (1988). Recent activity of the Iznik-Mekece fault at Corak Stream, east of Iznik. In Y. Honkura, A. M. Isikara (Eds.), *Multidisciplinary research on fault activity in the western part of the North Anatolian Fault Zone* (pp. 15–27). Tokyo: Institute of Technology.

Ikeda, Y., Herece, E., Sugai, T., & Isikara, A. M. (1991). Postglacial crustal deformation associated with slip on the western part of the North Anatolian Fault Zone in the Iznik Lake Basin, Turkey. *Bulletin of the Department of Geography University of Tokyo*, 23, 13–23.

Ikeda, Y., Suzuki, Y., & Herece, E. (1989). Late Holocene activity of the North Anatolian fault zone in the Orhangazi plain, northwestern Turkey. In Y. Honkura, A. M. Isikara (Eds.), *Multidisciplinary research on fault activity in the western part of the North Anatolian fault zone* (Vol. 2, pp. 16–30). Tokyo: Institute of Technology.

Ikeda, Y., Suzuki, Y., Herece, E., Saroglu, F., Isikara, A. M., & Honkura, Y. (1991). Geological evidence for the last two faulting events on the north Anatolian Fault zone in the Mudurnu Valley, western Turkey. *Tectonophysics*, 193(4), 335-345. https://doi.org/10.1016/0040-1951(91)90342-P

Ketin, I. (1969). Kuzey Anadolu Fayi Hakkinda. *Maden Tektik ve Arama Dergisi*, 72, 1-27.

Ketin, I., & Rösli, F. (1953). Makroseismische Untersuchungen über das nordwest-anatolische

Beben vom 18 März 1953. *Eclogae Geologicae Helvetiae*, 46, 187-208.

Kim, S. J., Koh, K., Boyd, S., & Gorinevsky, D. (2009). l1 trend filtering. *SIAM Review*, 51(2), 339-360. https://doi.org/10.1137/070690274

King, G., & Nabelek, J. (1985). Role of Fault Bends in the Initiation and Termination of Earthquake Rupture. *Science*, 228(4702), 984-987. DOI: 10.1126/science.228.4702.984

King., G., Klinger, Y., Bowman, D., & Tapponnier, P. (2005). Slip-Partitioned Surface Breaks for the M_w 7.8 2001 Kokoxili Earthquake, China. *Bulletin of the Seismological Society of America*, 95(2), 731-738. doi: 10.1785/0120040101

Klinger, Y. (2010). Relation between continental strike-slip earthquake segmentation and thickness of the crust. *Journal of Geophysical Research: Solid Earth*, 115, B07306.

Klinger, Y., Etchebes, M., Tapponnier, P., & Narteau, C. (2011). Characteristic slip for five great earthquakes along the Fuyun fault in China. *Nature Geoscience*, 4(6), 389–392. https://doi.org/10.1038/ngeo1158

Klinger, Y., Sieh, K., Altunel, E., Akoglu, A., Barka, A., Dawson, T., et al. (2003). Palaeoseismic Evidence of Characteristic Slip on the Western Segment of the North Anatolian Fault, Turkey. *Bulletin of the Seismological Society of America*, 93(6), 2317-2332. https://doi.org/10.1785/0120010270

Klinger, Y., Xu, X., Tapponnier, P., Van der Woerd, J., Lasserre, C., & King, G. (2005). High-Resolution Satellite Imagery Mapping of the Surface Rupture and Slip Distribution of the M_w ~7.8, 14 November 2001 Kokoxili Earthquake, Kunlun Fault, Northern Tibet, China. *Bulletin of the Seismological Society of America*, 95(5), 1970-1987. http://dx.doi.org/10.1785/0120040233

Koçyigit, A. (1988). Tectonic setting of the Geyve Basin: age and total displacement of the

Geyve Fault Zone. *Journal of Pure and Applied Sciences*, 21, 81–104.

Koçyigit, A. & Özacar, A. A. (2003). Extensional neotectonic regime through the NE edge of the outer Isparta Angle, SW Turkey: new field and seismic data. *Turkish Journal of Earth Sciences*, 12(1), 67–90.

Kozaci, Ö., Dolan, J. F., & Finkel, R. C. (2009). A late Holocene slip rate for the central North Anatolian fault, at Tahtaköprü, Turkey, from cosmogenic ^{10}Be geochronology: Implications for fault loading and strain release rates. *Journal of Geophysical Research: Solid Earth*, 114(B1), B01405. https://doi.org/10.1029/2008JB005760

Kozaci, Ö., Dolan, J. F., Finkel, R., & Hartleb, R. (2007). Late Holocene slip rate for the North Anatolian fault, Turkey, from cosmogenic 36Cl geochronology: Implications for the constancy of fault loading and strain release rates. *Geology*, 35(10), 867-870. https://doi.org/10.1130/G23187A.1

Kürçer, A., Chatzipetros, A., Tutkun, S. Z., Pavlides, S., Özkan Ates, & Valkaniotis, S. (2008). The Yenice–Gönen active fault (NW Turkey): Active tectonics and palaeoseismology. *Tectonophysics*, 453(1), 263 – 275. https://doi.org/10.1016/j.tecto.2007.07.010

Kürcer, A., Özalp, S., Özdemir, E., Uygun Güldogan, C., & Duman, T. Y. (2019). Active tectonics and paleoseismologic characteristics of the Yenice-Gönen fault, NW Turkey, in light of the 18 March 1953 Yenice-Gönen Earthquake (Ms=7.2). *Maden Tektik ve Arama Dergisi*, 159, 29-62. https://doi.org/10.19111/bulletinofmre.500553

Kurt, H., Sorlien, C.C., Seeber, L., Steckler, M.S., Shillington, D.J., Cifci, G., et al. (2013). Steady late quaternary slip rate on the Cinarcik section of the North Anatolian fault near Istanbul, Turkey. *Geophysical Research Letters*, 40, 4555-4559. doi:10.1002/grl.50882.

Kurtz, R., Klinger, Y., Ferry, M., & Ritz, J. F. (2018). Horizontal surface-slip distribution through several seismic cycles: The Eastern Bogd fault, Gobi-Altai, Mongolia. *Tectonophysics*, 734-735, 167-182. https://doi.org/10.1016/j.tecto.2018.03.011

Lafarge, T., & Possolo, A. (2016). The NIST Uncertainty Machine. *NCSLI Measure*, 10(3), 20-27. DOI: 10.1080/19315775.2015.11721732

Le Béon, M., Klinger, Y., Al-Qaryouti, M., Mériaux, A. S., Finkel, R., C., Elia, A., et al. (2010). Early Holocene and Late Pleistocene slip rates of the southern Dead Sea Fault determined from 10Be cosmogenic dating of offset alluvial deposits. *Journal of Geophysical Research: Solid Earth*, 115, B11414, doi:10.1029/2009JB007198.

Lefevre, M., Klinger, Y., Al-Qaryouti, M., Le Béon, M., & Moumani, K. (2018). Slip deficit and temporal clustering along the Dead Sea fault from palaeoseismological investigations. *Scientific Reports*, 8, doi:10.1038/s41598-018-22627-9.

Le Pichon, X., Imren, C., Rangin, C., Sengör, A. M. C., & Siyako, M. (2014). The South Marmara Fault. *International Journal of Earth Sciences*, 103(1), 219–231. https://doi.org/10.1007/s00531-013-0950-0

Lifton, N. (2016). Implications of two Holocene time dependent geomagnetic models for cosmogenic nuclide production rate scaling. *Earth and Planetary Science Letters*, 433, 257-268. https://doi.org/10.1016/j.epsl.2015.11.006

Lifton, N. A., Sato, T., & Dunai, T. J. (2014). Scaling in situ cosmogenic nuclide production rates using analytical approximations to atmospheric cosmic-ray fluxes. *Earth and Planetary Science Letters*, 386, 149-160. https://doi.org/10.1016/j.epsl.2013.10.052

Lin, Z., Liu-Zeng, J., Weldon II, R. J., Tian, J., Ding, C., & Du, Y. (2020). Modeling repeated

coseismic slip to identify and characterize individual earthquakes from geomorphic offsets on strike-slip faults. *Earth and Planetary Science Letters*, 545, 116313. https://doi.org/10.1016/j.epsl.2020.116313

Liu-Zeng, J., Klinger, Y., Sieh, K., Rubin, C., & Seitz, G. (2006). Serial ruptures of the San Andreas fault, Carrizo Plain, California, revealed by three-dimensional excavations. *Journal of Geophysical Research*, 111, B02306.

Lozos, J. C. (2016). A case for historic joint rupture of the San Andreas and San Jacinto faults. *Science Advances*, 2(3), e1500621. https://doi.org/10.1126/sciadv.1500621

Manighetti, I., Perrin, C., Dominguez, S., Garambois, S., Gaudemer, Y., Malavieille, J., et al. (2015). Recovering paleoearthquake slip record in a highly dynamic alluvial and tectonic region (Hope Fault, New Zealand) from airborne lidar. *Journal of Geophysical Research: Solid Earth*, 120(6), 4484–4509. https://doi.org/10.1002/2014JB011787

Manighetti, I., Perrin, C., Gaudemer, Y., Dominguez, S., Stewart, N., Malavieille, J., Garambois, S. (2020). Repeated giant earthquakes on the Wairarapa fault, New Zealand, revealed by Lidar-based paleoseismology. *Scientific Reports*, 10, 2124. https://doi.org/10.1038/s41598-020-59229-3

Martin, L. C. P., Blard, P.-H., Balco, G., Lavé, J., Delunel, R., Lifton, N., Laurent, V. (2017). The CREp program and the ICE-D production rate calibration database: A fully parameterizable and updated online tool to compute cosmic-ray exposure ages. *Quaternary Geochronology*, 38, 25-49. https://doi.org/10.1016/j.quageo.2016.11.006

McClusky, S., Balassanian, S., Barka, A., Demir, C., Ergintav, S., Georgiev, I., et al. (2000). Global Positioning System constraints on plate kinematics and dynamics in the eastern

Mediterranean and Caucasus. *Journal of Geophysical Research: Solid Earth*, 105(B3), 5695–5719.

McGill, S. F., & Rubin, C. M. (1999). Surficial slip distribution on the central Emerson fault during the June 28, 1992, Landers earthquake, California. *Journal of Geophysical Research: Solid Earth*, 104(B3), 4811–4833.

McGill, S. F., & Sieh, K. (1991). Surficial offsets on the Central and Eastern Garlock Fault associated with prehistoric earthquakes. *Journal of Geophysical Research*, 96(B13), 21597-21621.

Meade, B. J., Hager, B. H., McClusky, S. C., Reilinger, R. E., Ergintav, S., Lenk, O., et al. (2002). Estimates of seismic potential in the Marmara Sea region from block models of secular deformation constrained by Global Positioning System measurements. *Bulletin of the Seismological Society of America*, 92(1), 208–215. http://dx.doi.org/10.1785/0120000837

Merchel, S. & Herpers, U. (1999). An update on radiochemical separation techniques for the determination of long-lived radionuclides via accelerator mass spectrometry. *Radiochimica Acta*, 84(4), 215-219. https://doi.org/10.1524/ract.1999.84.4.215

Moratto, Z. M., Broxton, M. J., Beyer, R. A., Lundy, M., & Husmann, K. (2010). *Ames Stereo Pipeline, NASA's Open Source Automated Stereogrammetry Software*. Paper presented at the 41th Lunar and Planetary Science Conference, Woodlands, TX.

Motagh, M., Hoffmann, J., Kampes, B., Baes, M., & Zschau, J. (2007). Strain accumulation across the Gazikoy–Saros segment of the North Anatolian Fault inferred from Persistent Scatterer Interferometry and GPS measurements. *Earth and Planetary Science Letters*, 255, 432-444. http://dx.doi.org/10.1016/j.epsl.2007.01.003.

Onderdonk, N., McGill, S., & Rockwell, T. (2018). A 3700 yr paleoseismic record from the northern San Jacinto fault and implications for joint rupture of the San Jancinto and San Andreas faults. *Geosphere*, 14(6), 2447-2468. https://doi.org/10.1130/GES01687.1

Özalp, S., Emre, Ö., & Dogan, A. (2013). The segment structure of southern branch of the North Anatolian Fault and palaeoseismological behaviour of the Gemlik fault, NW Anatolia. *Bulletin of MTA*, 147, 1–17.

Özbey, V., Özeren, M.S., Henry, P., Klein, E., Galgana, G., Karabulut, H., et al. (2021). Kinematics of the Marmara Region: a fusion of continuum and block models. *Mediterranean Geoscience Reviews*, 3, 57-78. https://doi.org/10.1007/s42990-021-00051-y

Öztürk, K., Yaltirak, C., & Alpar, B. (2009). The relationship between the tectonic setting of the Lake Iznik Basin and the Middle Strand of the North Anatolian Fault. *Turkish Journal of Earth Sciences*, 18, 209–224.

Palyvos, N., Pantosti, D., Zabci, C., & D'Addezio, G. (2007). Paleoseismological Evidence of Recent Earthquakes on the 1967 Mudurnu Valley Earthquake Segment of the North Anatolian Fault Zone. *Bulletin of the Seismological Society of America*, 97(5), 1646-1661. https://doi.org/10.1785/0120060049

Parsons, T., Toda, S., Stein, R. S., Barka, A., & Dieterich, J. H. (2000). Heightened odds of large earthquakes near Istanbul: An interaction-based probability calculation. *Science*, 288(5466), 661–665. https://doi.org/10.1126/science.288.5466.661

Pondard, N., Armijo, R., King, G. C. P., Meyer, B., & Flérit, F. (2007). Fault interactions in the Sea of Marmara pull-apart (North Anatolian Fault): earthquake clustering and propagating earthquake sequences. *Geophysical Journal International*, 171, 1185-1197.

https://doi.org/10.1111/j.1365-246X.2007.03580.x

Reilinger, R., McClusky, S., Vernant, P., Lawrence, S., Ergintav, S., Cakmak, R., et al. (2006). GPS constraints on continental deformation in the Africa-Arabia-Eurasia continental collision zone and implications for the dynamics of plate interactions. *Journal of Geophysical Research: Solid Earth*, 111, B05411. doi:10.1029/2005JB004051.

Reitman, N. G., Mueller, K. J., Tucker, G. E., Gold, R. D., Briggs, R. W., & Barnhart, K. R. (2019). Offset channels may not accurately record strike-slip fault displacements: Evidence from landscape evolution models. *Journal of Geophysical Research: Solid Earth*, 124, 13,427-13,451.

Ren, Z., Zielke, O., & Yu, J. (2018). Active tectonics in 4D high-resolution. *Journal of Structural Geology*, 117, 264-271. https://doi.org/10.1016/j.jsg.2018.09.015

Rizza, M., Ritz, J. F., Braucher, R., Vassallo, R., Prentice, C., Mahan, S., et al. (2011). Slip rate and slip magnitudes of past earthquakes along the Bogd left-lateral strike-slip fault (Mongolia). *Geophysical Journal International*, 186(3), 897-927. https://doi.org/10.1111/j.1365-246X.2011.05075.x

Rockwell, T. K., Dawson, T. E., Young Ben-Horin, J., & Seitz, G. (2014). A 21-Event, 4,000 Year History of Surface Ruptures in the Anza Seismic Gap, San Jacinto Fault, and Implications for Long-term Earthquake Production on a Major Plate Boundary Fault. *Pure and Applied Geophysics*, 172, 1143-1165. https://doi.org/10.1007/s00024-014-0955-z

Rockwell, T. K., Lindvall, S., Dawson, T., Langridge, R., Lettis, W., & Klinger, Y. (2002). Lateral Offsets on Surveyed Cultural Features Resulting from the 1999 Izmit and Düzce Earthquakes, Turkey. *Bulletin of the Seismological Society of America*, 92(1), 79-94. https://doi.org/10.1785/0120000809

Rockwell, T., Ragona, D., Seitz, G., Langridge, R., Ersen Aksoy, M., Ucarkus, G., et al. (2009). Palaeoseismology of the North Anatolian Fault near the Marmara Sea: Implications for fault segmentation and seismic hazard. In K. Reicherter, A. M. Michetti, P. G. Silva (Eds.), *Palaeoseismology: Historical and Prehistorical Records of Earthquake Ground Effects for Seismic Hazard Assessment, Geological Society Special Publications* (Vol. 316(1), pp. 31-54). London: The Geological Society. https://doi.org/10.1144/SP316.3

Scharer, K. M., Salisbury, J. B., Arrowsmith, J. R., & Rockwell, T. K. (2014). Southern San Andreas Fault Evaluation Field Activity: Approaches to Measuring Small Geomorphic Offsets – Challenges and Recommendations for Active Fault Studies. *Seismological Research Letters*, 85, 68-76. https://doi.org/10.1785/0220130108

Schwartz, D. P., & Coppersmith, K. J. (1984). Fault Behavior and Characteristic Earthquakes: Examples From the Wasatch and San Andreas Fault Zones. *Journal of Geophysical Research*, 89(B7), 5681-5698.

Sengör, A. M. C., Grall, C., Imren, C., Le Pichon, X., Görür, N., Henry, P., et al. (2014). The geometry of the North Anatolian transform fault in the Sea of Marmara and its temporal evolution: implications for the development of intracontinental transform faults. *Canadian Journal of Earth Sciences*, 51(3), 222–242. https://doi.org/10.1139/cjes-2013-0160

Sengör, A. M. C., Tüysüz, O., Imren, C., Sakinç, M., Eyidogan, H., Görür, N., et al. (2005). The North Anatolian Fault: A New Look. *Annual Review of Earth and Planetary Sciences*, 33, 37-112. https://doi.org/10.1146/annurev.earth.32.101802.120415

Sengör, A. M. C., & Zabci, C. (2019). The North Anatolian Fault and the North Anatolian Shear Zone. In C. Kuzucuoglu, A. Ciner, N. Kazanci (Eds.), *Landscape and Landforms of Turkey* (pp.

481-494). Cham: Springer International Publishing. https://doi.org/10.1007/978-3-030-03515-0_27

Shean, D. E., Alexandrov, O., Moratto, Z., Smith, B. E., Joughin, I. R., Porter, C. C., & Morin, P. J. (2016). An automated, open-source pipeline for mass production of digital elevation models (DEMs) from very high-resolution commercial stereo satellite imagery. *ISPRS Journal of Photogrammetry and Remote Sensing*, 116, 101–117. https://doi.org/10.1016/j.isprsjprs.2016.03.012

Sieh, K. E. & Jahns, R. H. (1984). Holocene activity of the San Andreas fault at Wallace Creek, California. *Geological Society of America Bulletin*, 95(8), 883–896. https://doi.org/10.1130/0016-7606(1984)95<883:HAOTSA>2.0.CO;2

Sipahioglu, S. & Matsuda, T. (1986). Geology and Quaternary fault in the Iznik-Mekece area. In A. M. Isikara, Y. Honkura (Eds.), *Electric and Magnetic Research on Active Faults in the North Anatolian Fault Zone*. (pp. 25-41). Tokyo: Tokyo Inst. Technology.

Stein, R. S., Barka, A. A., & Dieterich, J. H. (1997). Progressive failure on the North Anatolian fault since 1939 by earthquake stress triggering. *Geophysical Journal International*, 128(3), 594–604. https://doi.org/10.1111/j.1365-246X.1997.tb05321.x

Straub, C., Kahle, H.-G., & Schindler, C. (1997). GPS and geologic estimates of the tectonic activity in the Marmara Sea region, NW Anatolia. *Journal of Geophysical Research: Solid Earth*, 102(B12), 27587–27601.

Stroeven, A. P., Heyman, J., Fabel, D., Björck, S., Caffee, M. W., Fredin, O., & Harbor, J. M. (2015). A new Scandinavian reference ^{10}Be production rate. *Quaternary Geochronology*, 29, 104–115. https://doi.org/10.1016/j.quageo.2015.06.011

Tanoglu, A., & Erinc, S. (1956). Garsak bogazı ve Eski Sakarya (The Garsak gorge and the Sakarya River diversion). *Istanbul Universitesi Cografya Enstitusu Dergisi*, 4, 17–31.

Tsukuda, T., Satake, K., Honkura, Y., Üçer, S. B., & Isikara, A. M. (1988). Low seismicity, low coda-Q and discontinuities of the upper crust in the vicinity of the Iznik-Mekece fault, the North Anatolian Fault Zone, Turkey. *Bulletin of Earthquake Research of the Institute University of Tokyo*, 63, 327–348.

Uppala, S. M., KÅllberg, P. W., Simmons, A. J., Andrae, U., Bechtold, V. D. C., Fiorino, M., et al. (2005). The ERA-40 re-analysis. *Quarterly Journal of the Royal Meteorological Society*, 131, 2961-3012. https://doi.org/10.1256/qj.04.176

van der Woerd, J., Klinger, Y., Sieh, K., Tapponnier, P., Ryerson, F. J., & Mériaux, A. S. (2006). Long-term slip rate of the southern San Andreas Fault from ^{10}Be-^{26}Al surface exposure dating of an offset alluvial fan. *Journal of Geophysical Research*, 111, B04407.

Vardar, D., Öztürk, K., Yaltırak, C., Alpar, B., & Tur, H. (2014). Late Pleistocene-Holocene evolution of the southern Marmara shelf and sub-basins: middle strand of the North Anatolian fault, southern Marmara Sea, Turkey. *Marine Geophysical Research*, 35(1), 69-85. https://doi.org/10.1007/s11001-013-9210-8

Ward, S. N. (1997). Dogtails versus rainbows: synthetic earthquake rupture models as an aid in interpreting geological data. *Bulletin of the Seismological Society of America*, 87(1), 1422-1441.

Wechsler, N., Rockwell, T. K., & Klinger, Y. (2018). Variable slip-rate and slip-per-event on a plate boundary fault: The Dead Sea fault in northern Israel. *Tectonophysics*, 722, 210-226. https://doi.org/10.1016/j.tecto.2017.10.017

Wells, D. L., & Coppersmith, K. J. (1994). New Empirical Relationships among Magnitude,

Rupture Length, Rupture Width, Rupture Area, and Surface Displacement. *Bulletin of the Seismological Society of America*, 84(4), 974-1002.

Wesnousky, S. G. (2006). Predicting the endpoints of earthquake ruptures. *Nature*, 444, 358-360. https://doi.org/10.1038/nature05275

Yılmaz, Y., Genç, C., Yigitbas, E., Bozcu, M., & Yılmaz, K. (1995). Geological evolution of the late Mesozoic continental margin of Northwestern Anatolia. *Tectonophysics*, 243(1), 155–171. https://doi.org/10.1016/0040-1951(94)00196-G

Yoshioka, T. & Kusçu, I. (1994). Late Holocene faulting events on the Iznik-Mekece fault in the western part of the North Anatolian fault zone, Turkey. *Bulletin of the Geological Survey of Japan*, 45(11), 677–685.

Zabcı, C. (2019). Spatio-temporal behaviour of continental transform faults: Implications from the late Quaternary slip history of the North Anatolian Fault, Turkey. *Canadian Journal of Earth Sciences*, 56(11), 1218-1238. https://doi.org/10.1139/cjes-2018-0308

Zabci, C., Sançar, T., Akyüz, H. S., & Kiyak, N. G. (2015). Spatial slip behavior of large strike-slip fault belts: Implications for the Holocene slip rates of the eastern termination of the North Anatolian Fault, Turkey. *Journal of Geophysical Research: Solid Earth*, 120(12), 8591-8609.

Zielke, O. (2018). Earthquake Recurrence and the Resolution Potential of Tectono-Geomorphic Records. *Bulletin of the Seismological Society of America*, 108(3A), 1399-1413. https://doi.org/10.1785/0120170241

Zielke, O., Arrowsmith, J. R., Grant Ludwig, L., & Akçiz, S. O. (2010). Slip in the 1857 and earlier large earthquakes along the Carrizo Plain, San Andreas Fault. *Science*, 327, 1119-1122. https://doi.org/10.1126/science.1182781

Zielke, O., Arrowsmith, J. R., Grant Ludwig, L., & Akciz, S. O. (2012). High-Resolution Topography-Derived Offsets along the 1857 Fort Tejon Earthquake Rupture Trace, San Andreas Fault. *Bulletin of the Seismological Society of America*, 102(3), 1135-1154. https://doi.org/10.1785/0120110230

Zielke, O., Klinger, Y., & Arrowsmith, J. R. (2015). Fault slip and earthquake recurrence along strike-slip faults - Contributions of high-resolution geomorphic data. *Tectonophysics*, 638, 43–62. https://doi.org/10.1016/j.tecto.2014.11.004